A. Frezzotti, P.F. Barbante
Simulation of Shock Induced Vapor Condensation Flows in the Lennard-Jones Fluid by Microscopic and Continuum Models
Physics of Fluids, Vol. 32, N. 12, 2020, 122106 (11 pages)
doi:10.1063/5.0032439

Simulation of shock induced vapor condensation flows in the Lennard-Jones fluid by microscopic and continuum models

A. Frezzotti[1] and P. Barbante[2]

[1)]*Politecnico di Milano, Dipartimento di Scienze e Tecnologie Aerospaziali*

Via La Masa, 34 - 20156 Milano - Italy[a)]

[2)]*Politecnico di Milano, Dipartimento di Matematica*

Via Bonardi, 9 - 20133 Milano - Italy[b)]

(Dated: 18 November 2020)

The vapor condensation onto a thin liquid film, induced by the reflection of a weak shock wave, is studied by Molecular Dynamics atomistic simulations of a simple Lennard-Jones fluid. Molecular Dynamics results provide reference flowfields for two models. The first one adopts a hybrid continuum-kinetic description in which the liquid phase is described by hydrodynamic equations, whereas the vapor is described by the Boltzmann equation. The structureless liquid-vapor interface is replaced by a classical kinetic boundary condition. The second model is based on the Diffuse Interface full continuum description of the Lennard-Jones fluid liquid, vapor and interface regions. For both models, the required fluid thermodynamic and transport properties have been prescribed according to those of Lennard-Jones fluid. Not unexpectedly, results show that the continuum-kinetic model provides a good description of Molecular Dynamics results when the vapor is close to ideal conditions, increasingly deviating from reference data when the vapor non-ideality increases. The opposite behavior is found for the Diffuse Interface model. It is observed that flow conditions exist where both models fail to provide a reasonably accurate description of reference flow properties.

[a)]Electronic mail: aldo.frezzotti@polimi.it

[b)]Electronic mail: paolo.barbante@polimi.it

I. INTRODUCTION

The present work, which completes a previous study[1], aims at assessing the capabilities of kinetic and continuum models to describe evaporation and condensation phenomena in simple fluids[2,3], when the vapor phase can be no longer considered dilute or ideal. This condition is of interest in the study of fuel droplets evaporation[4] and explosive boiling[5]. If compared with the large number of papers, devoted to clarify the role of kinetic effects in evaporation/condensation phenomena involving a a dilute vapor phase[6,7], the assessment of kinetic effects on dense vapor flow is much less developed. In recent papers, the weak evaporation of a liquid film in presence of a dense vapor[8] and the formulation of kinetic boundary conditions for high pressure vapors[9] have been studied by Enskog-Vlasov kinetic model[10,11]. Although Enskog-Vlasov equation proved to be a quite useful model to investigate two-phase flows with kinetic effects[12–14], it has been decided to base this still exploratory investigation of the effects of vapor non-ideality on evaporation/condensation flows on the more realistic Lennard-Jones fluid[15].

The selected test flow configuration to be simulated consists in the vapor condensation onto a thin liquid film, initially in equilibrium with its vapor, at a prescribed temperature. Condensation is induced by the vapor pressure and temperature increase following the reflection of a weak shock wave, initially propagating through the vapor to impinge on the liquid surface. Shock reflection from liquid films is a convenient way to study condensation processes, not only from the numerical but also from the experimental point of view. The technique has been extensively studied and used to obtain experimental condensation coefficients of various liquids[16,17]. It is also to be noted that vapor non-ideality is more easily produced and controlled in condensation than in evaporation flows where liquid surface cooling tends to reduce the vapor pressure and bring flow conditions closer to ideal. As explained below, the present study of condensation flows in a dense vapor is based on the comparison of a set of non-equilibrium Molecular Dynamics[18] simulations of the Lennard-Jones fluid, at increasing initial temperatures, with the companion results of two different models. The thermodinamic and transport properties required by the models formulation have been assigned to match the corresponding properties of the Lennard-Jones fluid for a wide range of fluid density and temperature. The first one is based on a mixed continuum-kinetic fluid description, the second is based on a classical Diffuse Interface model[19]. The first one describes the vapor as an ideal gas, governed by the Boltzmann equation[20] and it is expected to match Molecular Dynamics results at low temperature when the vapor is nearly ideal[21]. The second one is known

to fail predicting low temperature evaporation rates, lacking the capability of describing Knudsen layers[21]. However, it is expected to provide a good description of Molecular Dynamics results when the vapor density increases and kinetic effects play a negligible role. As shown below, the two models help framing flow conditions in which kinetic effects shold be extended to non-ideal fluids or Diffuse Interface models shold be extended to deal with kinetic regions. According with paper aims, the following content is organized as follows: Section II describes the problem formulation, Section III describes the models used to study the test problem, whereas results and comparisons are presented in Section IV. Finally, Section V presents concluding remarks.

II. PROBLEM FORMULATION

The following problem formulation is taylored on the MD description and simulations setup, depicted in Fig. 1. When studying the *same* system by the hybrid hydrodynamic-kinetic model (HM) and diffuse interface model (DIM), domains and boundary conditions will be modified, as required by each model pecularities.

At time $t = 0$, a planar, infinite liquid slab, of nominal thickness Δz^0 occupies the spatial domain $\mathscr{S}^0 = \{(x,y,z) \in R^3 : -\frac{\Delta z^0}{2} \leq z \leq \frac{\Delta z_0}{2}\}$ in the laboratory reference frame. The liquid slab is assumed to be initially in equilibrium with its vapor phase at temperature T^0. The vapor phase occupies the region $\mathscr{V}^0 = \{(x,y,z) \in R^3 : \frac{\Delta z_0}{2} < |z| < Z_p^0\}$, union of the two gaps symmetrically located with respect to the origin and delimited by the liquid-vapor interfaces and two infinite, planar and perfectly reflecting pistons, initially located at $\mp Z_p^0$, respectively. At time $t = 0$, the pistons are impulsively set into a uniform motion with subsonic velocities $\pm V_p$ towards the interfaces. The vapor compression produces two shock waves traveling towards the interfaces with constant supersonic speed, with respect to the unshocked vapor. The properties of the fully developed shocks are determined by V_p through the Rankine-Hugoniot relationships. The interaction of shocks with liquid surfaces causes the heating of the liquid slab and the reflection of the impinging shocks towards the pistons. In order to control the temperature field in liquid, the center of the liquid slab is kept at constant temperature T^0. After the reflected shock is fully formed, each vapor region can be divided into a thin Knudsen layer, next to the interface, and a uniform equilibrium region of increasing thickness, behind the reflected shock. Here, the temperature T_c and pressure P_c are higher than in the initial equilibrium state, thus causing the vapor to condense onto the liquid surface with subsonic velocity V_c. If the initial slab thickness and width of the

TABLE I. Equilibrium LJ fluid properties

T^0	ρ_l	ρ_v	λ_v	$Z = p/\rho_v T^0$
0.72	0.803	$5.49e-03$	21.60	0.953
0.80	0.761	$1.226e-02$	11.46	0.914
0.90	0.706	$2.793e-02$	4.785	0.844
1.00	0.641	$5.705e-02$	2.473	0.744

vapor gaps are properly chosen, the evolution of the system following shock reflection consists in a fairly uniform increase of the slab thickness, due to quasi-steady condensation. Actually, the temperature profile in the liquid slab, after a short transient phase, takes an almost linear shape determined by T^0, the nearly constant temperature $T_i(t)$ of the interface and the slowly evolving slab thickness $\Delta z(t)$. In this quasi-steady subsonic condensation flow, T_c, P_c and the Mach number M_c are related by a relationship of the form $\frac{P_c}{P_{sat}(T_i)} = F_{sub}(\frac{T_c}{T_i}, M_c)$[7]. The form of the function F_{sub}, has been determined from kinetic theory, for a dilute monatomic[7] and polyatomic gas[22]. The condensation rate and the reflected shock properties, crucially depends on the mass, momentum and energy transport through the interfaces[7,23], hence the problem provides a useful test bench to investigate the capabilities of models to describe such processes.

Table I lists equilibrium values of the liquid density ρ_l and the the vapor density ρ_v as a function of a few selected values of the temperature T, along the coexistence line of the Lennard-Jones (LJ) $6-12$ fluid[15], adopted in this study.

As is well known, LJ fluid consists in an ensemble of structureless point atoms of mass m interacting by the central potential

$$\phi_{LJ}(r) = 4\varepsilon\left[\left(\frac{\sigma}{r}\right)^{12} - \left(\frac{\sigma}{r}\right)^{6}\right] \tag{1}$$

In Eq. (1), r the distance between two interacting atoms, ε is the depth of the potential well, whereas the length σ defines the effective range of atomic forces. Interatomic forces derived by the $\phi_{LJ}(r)$ are directly used in the MD simulations described below. HM and DIM descriptions of the LJ fluid are based on its thermodynamic and transport properties, respectively obtained from Ref. 24 and Refs. 25–27. When necessary, corrections have been applied to take into account the potential cutoff used in MD simulations. As in the rest of the paper, data are given in LJ units: lenght is normalized to σ, time is normalized to $\sigma\sqrt{\frac{m}{\varepsilon}}$ and mass to m. Table I also provides values of the vapor phase mean free path λ_v and compressibility $Z = P_{LJ}(\rho_v, T)/\rho_v T$ as a function

TABLE II. Incident shock properties as functions of unshocked gas temperature and piston speed. ρ_{is} and T_{is} respectively denote the density and temperature behind the piston generated shock, prior to shock reflection. V_{is} is the incident shock propagation velocity. Values within brackets refer to ideal, monatomic gas theory.

T^0	V_p	$\frac{\rho_{is}}{\rho_v}$	$\frac{T_{is}}{T^0}$	V_{is}
0.72	0.2	1.197 (1.193)	1.1280 (1.1263)	1.2130 (1.2368)
0.80	0.2	1.1909 (1.1825)	1.1239 (1.1196)	1.252 (1.2957)
0.90	0.2	1.1842 (1.1716)	1.1125 (1.1206)	1.2865 (1.3653)
1.00	0.2	1.1810 (1.1624)	1.1213 (1.1065)	1.311 (1.4311)

of T^0. The latter quantity provides a measure of the deviation of the vapor phase from the ideal gas behavior. The mean free path λ_v has been estimated from from the vapor shear viscosity μ, following the dilute gas expression for hard sphere interaction[28]:

$$\lambda_v = \frac{16\mu}{5\sqrt{2\pi R T^0}\rho_v} \tag{2}$$

Although the concept of mean free path is strictly applicable only in the dilute gas limit, forcing the application of Eq. (2) out its validity range provides a second, useful indication about the vapor phase non-ideality, in addition to Z. The four equilibrium conditions listed in Table I have been chosen to provide flow conditions ranging from near ideal to non-ideal, according with the aims of the investigation.

Pistons velocity V_p has been set equal to 0.2 (in units of $\sqrt{\varepsilon/m}$) for all simulations, in order to generate a shock which is weak enough to cause a modest temperature change in the liquid phase but, at the same time, strong enough to be detected in the noisy MD simulations results of the vapor phase.

Table II lists the values of the ratios ρ_{is}/ρ_v and T_{is}/T^0 as well as of the incident shock propagation velocity V_{is} in the vapor at rest, before reflection at interfaces occurs. Shock properties have been obtained by the numerical solution of the Rankine-Hugoniot relationships[29] of the LJ vapor, using the thermodynamic properties given in Ref. 24. For reference, the properties computed in the limit of an ideal monatomic gas are also given, within brackets. Comparisons of the LJ values with their corresponding ideal gas approximations shows slightly smaller propagation velocity and larger density and temperature jumps across the shock.

III. DESCRIPTION OF MATHEMATICAL AND NUMERICAL MODELS

This section is devoted to a succint description of the mathematical and numerical models and tools, used to study the shock induced condensation in the flow geometry and conditions described above. A detailed description, in particular of HM and DIM numerical treatment, has been given in Ref. 21, where the evaporation of a liquid film in the dilute vapor regime has been investigated by the same tools.

A. Molecular Dynamics

In this work, MD simulations are required to provide reference data to be used in the assessment of HM and DIM capabilities to describe the same system.

Simulations have been performed by a MD code developed by one of authors (AF) and extensively validated against literature data[30]. The motion of N_a atoms, interacting by the potential $\phi_{LJ}(r)$ is computed numerically by integrating Newton's equations by the classical velocity Verlet scheme[31]. The infinite system described above is approximated as the union of an infinite number of periodic replicas of a finite, rectangular fluid column of fixed side lengths L_x and L_y along the two directions x and y, where periodic boundary conditions[31] are applied, being parallel to the liquid-vapor interfaces. The column extension along the direction normal to the interfaces, spanned by the coordinate z, is delimited by the piston positions. The interaction of fluid atoms with the pistons is described by purely repulsive, short range forces, normal to the planar piston surfaces. More precisely, the force fields $F_z^{(\mp)}$ that left and right piston, respectively located at $\mp Z_p(t)$, exert on fluid atoms are given by the following expression:

$$F_z^{(\mp)} = \varepsilon\sigma^{12}\frac{1}{[z \pm Z_p(t)]^{13}} \tag{3}$$

Expressions (3) have been derived by the repulsive contribution of a one-dimensional $6-12$ Lennard-Jones potential. The two parameters ε and σ have been assigned the same values (one, in reduced LJ units) used for atomic interactions.

Interatomic forces have been computed according to the minimum image convention[31], after truncating atomic interactions of pairs whose relative distance r exceeds a specified cut-off radius r_c. A spatial grid, with a cell size of r_c, has been used to index atoms and make the search of nearest neighbors more efficient. Simulations of condensation have been performed by starting each computation from an initial state in which a liquid slab, located in the center of the computational box,

is in equilibrium with its vapor at a specified temperature T^0. During non-equilibrium simulations, a narrow central strip of the liquid slab is thermostatted at temperature T^0 by a simple Gaussian thermostat[31]. Local values of the fluid macroscopic quantities have been obtained by sampling microscopic states of atoms belonging to the same spatial cell. The cell system for macroscopic quantities estimation is not the same used for atom indexing, having a resolution of a small fraction of σ. The time evolution of the system macroscopic properties has been obtained by dividing the total simulation duration into a number of time windows and computing time averaged system properties in each window. The amplitude of the time window is small enough to make the interface motion have a negligible effect on sampling spatial profiles. To further increase the number of microscopic samples in the vapor phase, each time frame has been obtained by superposing the results of 48 statistically independent parallel simulations of the (macroscopically) same system. The LJ potential cut-off radius, r_c, has been set equal to 3.0σ to keep the computational time within reasonable limits. The simulation box lengths L_x and L_y have been set equal to $8r_c$ (or 24σ) for $T^0 = 0.72, 0.8$ and reduced to $6r_c$ for $T^0 = 0.9$ and to $4r_c$ for $T^0 = 1.0$, where the denser vapor phase allows for smaller simulation boxes. The number of atoms used in each of the 48 statistical samples ranged from 42000 to 64000.

B. Diffuse interface model description

Including a DIM, in the present study of condensation flows, is suggested by the consideration that kinetic effects in the vicinity of the liquid-vapor interface should gradually disappear when the vapor phase density increases. Hence, it is expected that a hydrodynamic model might provide a good description of flow properties.

As is well known[19,32,33], the classical set of Navier-Stokes-Fourier equations can be given the capability to describe interfacial phenomena by adding Korteweg's capillary contribution to the the stress tensor of a viscous fluid. More precisely, DIM is obtained from the following general set of conservation laws:

$$\frac{\partial \rho}{\partial t} + \nabla \cdot (\rho \vec{v}) = 0 \tag{4}$$

$$\frac{\partial \rho \vec{v}}{\partial t} + \nabla \cdot (\rho \vec{v} \otimes \vec{v} + \mathbf{P}) = 0 \tag{5}$$

$$\frac{\partial \rho e_T}{\partial t} + \nabla \cdot (\rho e_T \vec{v} + \mathbf{P} \cdot \vec{v} + \vec{q}) = 0 \tag{6}$$

by adopting the closures:

$$\mathbf{P} = \mathbf{P}^{(s)} + \boldsymbol{\tau} \tag{7}$$

$$\boldsymbol{\tau} = -\mu\left(\nabla\vec{v} + \nabla\vec{v}^{T}\right) - \eta\left(\nabla\cdot\vec{v}\right)\mathbf{I} \tag{8}$$

$$\mathbf{P}^{(s)} = \left(p - K\rho\nabla^2\rho - \frac{1}{2}K|\nabla\rho|^2\right)\mathbf{I} + K\nabla\rho\otimes\nabla\rho \tag{9}$$

$$\rho e_T = \rho e + \frac{1}{2}K|\nabla\rho|^2 + \frac{1}{2}\rho v^2 \tag{10}$$

$$\vec{q} = -\kappa\nabla T + K\rho\left(\nabla\cdot\vec{v}\right)\nabla\rho \tag{11}$$

In Equations (7-11), ρ, T, $\vec{v}$, $p(\rho,T)$ and $e(\rho,T)$ are the fluid density, temperature, velocity, hydrostatic pressure and internal energy per unit mass, respectively. The total stress tensor $\mathbf{P}$ is written as the sum of the viscous contribution $\boldsymbol{\tau}$ and the static contribution $\mathbf{P}^{(s)}$. In the viscous part, $\mu(\rho,T)$ and $\eta(\rho,T)$ are the fluid shear and volume viscosity coefficients, respectively. The expression of $\mathbf{P}^{(s)}$ contains Korteweg's capillary stresses correction to the pure hydrostatic pressure, which depends on density spatial derivatives, its intensity being determined by the function $K(\rho,T)$. Consistency with thermodinamics requires that terms associated with density gradients are also added to the total energy density ρe_T definition in Equation (10) and to the classical Fourier contribution $-\kappa\nabla T$ in Equation (11) to obtain the total heat flux $\vec{q}$, being $\kappa(\rho,T)$ the fluid thermal conductivity.

In order to make the DIM consistent with the properties of the Lennard-Jones (LJ) fluid, the equations of state $p = p(\rho,T)$ and $e = e(\rho,T)$ have been computed from the modified Benedict-Webb-Rubin form, proposed in Ref. 24, which allows a very good approximation of the LJ fluid equilibrium MD data in a wide range of density and temperature. Simple mean field corrections allow accurately taking into account the effects of the LJ potential cutoff on thermodynamic properties of the LJ fluid[24]. Shear viscosity $\mu(\rho,T)$ and thermal conductivity $\kappa(\rho,T)$ have been computed from the expressions given in Ref. 25 and Ref. 26, respectively. The contribution of volume viscosity to normal stresses has been neglected because the results suggested that vapor expansion/compression occurs mainly in the low density flow region where volume viscosity is small. A second simplification, made in many DIM based studies, consists in assuming the coefficient $K(\rho,T)$ to be independent from ρ and T, although its value has been made to depend on T^0. For each computed solution, $K(T^0)$ has been obtained by matching the MD computed equilibrium density profile with the DIM equilibrium density profile. In spite of the simplification, excellent agreement between equilibrium DIM and MD density profiles is obtained by a proper choice of

$K(T^0)$[21]. It is also to be noted that little changes in the predicted flow properties have been found when non constant K functions have been considered, in a previuos study[21].

The governing equations (4), (5) and (6) are discretized in a fixed size domain by the finite volume method described in Ref. 21. In the discretized DIM formulation, the mirror symmetry of the MD domain has been exploited to compute flow properties in the positive half space $z > 0$. The numerical piston, used in MD simulations, has been replaced by inflow boundary conditions for density temperature and velocity, whose values are assigned the same values ρ_{is}, T_{is} and $-V_p$ of the companion MD simulations. The domain extension has been set wide enough to allow the propagation of the incident shock and to ensure the onset of a quasi-steady flow behind the reflected shock, before the latter reaches the boundary.

C. Hybrid continuum-kinetic model

At variance with MD and DIM which provide a unified description of the fluid, the model described below is based on separate descriptions of the liquid and vapor phases. The presence of a structurless interface is described by a kinetic boundary condition involving the distribution function of the vapor phase and the physical state of the liquid surface. As in the case of DIM, flow properties are computed in the half-space $z > 0$, by a spatially one-dimensional, unsteady formulation of the model. More precisely, the computional domain consists in the interval $0 < z < Z_p(t)$, being $Z_p(t)$ the postion of a specularly reflecting piston, moving toward the interface, with velocity $-V_p$. The interval is divided into the liquid region, extending from $z = 0$ to $z = Z_i(t)$, and the vapor region, extending from the interface position, $z = Z_i(t)$, to $Z_p(t)$.

The fluid flow in the vapor region is described by the following unsteady, one-dimensional Boltzmann equation for a dilute gas of hard spheres of diameter σ_{hs}[20]:

$$\frac{\partial f}{\partial t} + \xi_z \frac{\partial f}{\partial z} = \frac{\sigma_{hs}^2}{2} \int \left[f(z,\xi_1^*,t) f(z,\xi^*,t) - f(z,\xi_1,t) f(z,\xi,t) \right] \|\hat{\mathbf{k}} \circ \xi_r\| \, d^2\hat{\mathbf{k}} \, d\xi_1. \qquad (12)$$

In Eq. (12), $\hat{\mathbf{k}}$ is a unit vector which assigns the relative position of two colliding atoms at the time of their impact with velocities ξ, ξ_1 and relative velocity $\xi_r = \xi_1 - \xi$. The velocities ξ^* and ξ_1 respectively transform into ξ, ξ_1 in a restituting collision[20] according to the following expressions:

$$\xi^* = \xi + (\hat{\mathbf{k}} \circ \xi_r)\hat{\mathbf{k}}, \qquad \xi_1^* = \xi_1 - (\hat{\mathbf{k}} \circ \xi_r)\hat{\mathbf{k}} \qquad (13)$$

The value of hard sphere diameter σ_{hs} has been computed from the LJ viscosity at temperature T^0. This simplifying choice has been dictated by the observation that (a) temperature variations are

small in the present flow settings and (b) Knudsen layer structure does not seem to be very sensitive to the assumed intermolecular potential once transport properties values have been assigned[34].

HM results presented here have been obtained from solving Eq. (12) by a quite standard DSMC scheme[35] on a regular spatial grid, following the interface motion. The grid size has been set equal to $\lambda_v/10$ and not less than three millions simulation particles have been used to obtain the necessary sample size in an unsteady flow.

The liquid film in the domain $0 < z < Z_i(t)$ is described by the energy equation:

$$\rho C_p \frac{\partial T}{\partial t} = \frac{\partial}{\partial z}\left(\kappa \frac{\partial T}{\partial z}\right) \tag{14}$$

Eq. (14) is solved by assigning the constant temperature $T(0,t) = T^0$ in the center of the liquid slab and the energy flux at $z = Z_i(t)$, obtained by the relationship:

$$-\kappa \frac{\partial T}{\partial z} - \rho V_i e(\rho, T) = \frac{m}{2} \int \xi^2 (\xi_z - V_i) f(Z_i, \xi, t)\, d\xi \tag{15}$$

expressing equality of energy fluxes on the liquid and vapor sides of the interface whose velocity is $V_i(t) = \dot{Z}_i(t)$. Eq. (14) is supplemented with the following simplified form of the balance of momentum equation in the z direction:

$$P_{zz}(t) = p(\rho, T) = m \int \xi_z (\xi_z - V_i) f(Z_i, \xi, t)\, d\xi \tag{16}$$

and by the following interfacial mass balance equation, which determines $V_i(t)$:

$$-\rho(Z_i, t) V_i = \dot{m} = m \int (\xi_z - V_i) f(Z_i, \xi, t)\, d\xi. \tag{17}$$

In deriving Eq. (17), it has been assumed that the tiny velocity field in the liquid, caused by its thermal expansion/contraction, can be neglected. To derive Eq. (16), it has additionally been assumed that, due to the slow time evolution of liquid properties, the pressure in the liquid is uniform and equal to the momentum flux at the vapor liquid boundary. Finally, the coupling between the liquid and vapor phases is completed by the following kinetic boundary condition for the Boltzmann equation, at $z = Z_i(t)$.

$$f(Z_i, \xi, t) = \frac{\sigma_c n_s(T_i) + (1 - \sigma_c) n^-}{(2\pi R T_i)^{3/2}} \exp\left\{-\frac{\xi^2}{2RTi}\right\}, \quad \xi_z > 0 \tag{18}$$

$$n^- = \sqrt{\frac{2\pi}{RT_i}} \int (\xi_z - V_i) f(Z_i, \xi, t)\, d\xi, \quad \xi_z < V_i \tag{19}$$

According to a quite standard formulation of molecular scattering and emission at the liquid-vapor interface, Eqs. (18,19) are based on the assumption that both spontaneously evaporating and reflected molecules have a Maxwellian distribution, characterized by the interface temperature $T_i(t)$,

the saturated vapor density $n_s(T_i)$ and the evaporation/condensation coefficient σ_c[23], which determines the fraction $1-\sigma_c$ of total impinging flux (given by Eq. (19)) which is reflected back to the vapor phase.

It should be observed that the velocity of the interface V_i appears in the expression of the vapor flux impinging on the interface (see Eq. (19)), to take into account the motion of the vapor-liquid boundary. However, no drift velocity has been considered in the Maxwellian distribution function of spontaneously evaporating atoms, as given by Eq. (18), since the liquid bulk, from which evaporating atoms are emitted, is macroscopically at rest, as shown in Figs. 5, 8, 11. The velocity of the interface is not related to the mean velocity of the liquid bulk behind the interface, but it is the result of vapor deposition, in the case of condensation, or removal of molecular layers from a liquid at rest, in the case of evaporation. Actually, the half-space Maxwellian distribution function in Eq. 18 has been found to provide a very good fit of MD simulations of evaporation into vacuum, where the interface recedes (see Ref. 30 and references therein). That said, it should also be observed that the particular Maxwellian form in Eq. (18) is justified in equilibrium conditions, but it could deviate from the actual distribution function out of equilibrium. Non-Maxwellian distribution function shapes have been observed and/or proposed in several studies[12,36–38]. Assessing the effects of non-Maxwellian molecular evaporation flux goes beyond the aims of the present work where the simplest evaporation model has been considered, for the moment.

Equation (14) is solved numerically by a simple finite volume scheme on a grid whose cell boundaries move, following the thermal deformation of the liquid. All cells, except the boundary cell in contact with the vapor, contain a constant amount of liquid mass. The size, and mass of the boundary cell are updated according to Eq. (17). When its size, because of vapor condensation, exceeds a given threshold, the boundary cell is split into two cells conserving mass and energy. The discretized temperature and density fields are updated in two steps. First, a provisional temperature field is computed taking into account energy conduction, according to Eq. (14). Then, final values of density and temperature are computed according to local adiabatic transformations which produce the same pressure in each space cell. At the end of this second step, the positions of cell boundaries are updated, taking into account of mass conservation.

IV. RESULTS AND COMPARISONS

This section is devoted to describing and discussing the results obtained by the three models presented in the previous sections. As stated above, the role of Molecular Dynamics is to provide benchmark solutions, although affected by statistical noise. The kinetic model is expected to provide a good description of the flow when the vapor is close to ideal conditions, whereas the diffuse interface model is expected to perform well when vapor density increases.

Before presenting more detailed comparisons, based on the profiles of macroscopic quantities, it is interesting to compare the time evolution of the liquid-vapor interface position $Z_i(t)$ during the condensation process. In the case of MD and DIM, $Z_i(t)$ has been obtained as the position of the maximum of $||\frac{\partial \rho}{\partial z}(z,t)||$.

Figure 2 shows the displacements of the liquid-vapor interface during the condensation process following the incident shock impingement on the liquid surface. Results refer to MD, HM and DIM simulations in which the initial equilibrium temperature T^0 takes the values $0.72, 0.8, 0.9, 1.0$, respectively. The nominal initial liquid film thickness, obtained from the position where the density profiles has the maximal slope, is respectively equal to $57.8, 54.2, 80.2, 68.2$. Piston speed V_p has been set equal to 0.2 in all four cases presented here. A number of similar simulations with different combinations of liquid film thickness and piston speed settings have been performed and showed similar behaviors as to the comparison of HM and DIM with respect to MD reference data.

In each panel of Figure 2, the curves obtained by the different models have been synchronized (time shifted) on the MD condensation onset, marked by the initial $Z_i(t)$ ramp, following the constant equilibrium value. Synchronization is not strictly necessary but convenient to compare interface displacements after shock impingement. HM and DIM have, in general, their own different shock arrival time. The former because the ideal shock propagation velocity differs from the non-ideal one, the latter because each DIM simulation starts with a shock already formed at some distance from the interface.

Inspecting the four panels of Figure 2 shows that HM well reproduces the time evolution of the interface displacement computed by MD, at $T = 0.72$. For this particular case, a sensitivity analysis of the effects of the condensation coefficient σ_c has been conducted. The results show that the closest agreement with MD data is obtained for $\sigma_c = 1$. It is to be noted that the simulated condensation flows exhibit stronger sensitivity to σ_c than the evaporation flows studied in Ref. 21.

There, reference MD data could be matched by HM simulations, with comparable accuracy, in the range $0.8 \leq \sigma_c \leq 1$.

As T^0 is increased, vapor non-ideality causes HM results to increasingly deviate from MD data. The opposite behavior is observed for DIM simulations which, as it happened for evaporation flows[21], give a poor description of low density vapor flows. However, the discrepancies between DIM and MD reduce as T^0 is increased and, for $T^0 > 0.8$, DIM is more accurate than HM, although some deviation still persists at $T^0 = 1.0$. The following comparisons of density, temperature and velocity profiles provide further insight about the predictions of HM and DIM. Figures 3-11 show flowfield profiles taken at a time when the reflected shock is fully developed and the interface is advancing with nearly constant velocity, as shown in Fig. 2. In view of the indications given by the evolution of the interface displacements, only profiles of the cases $T^0 = 0.72, 0.9, 1.0$ will be shown. The two extreme T^0 values are representatives of cases where either the kinetic or the continuum model shows good agreement with reference data. The intermediate value $T^0 = 0.9$ represents a case where more or less pronounced deviations from reference data are present both in the kinetic and continuum description. Figure 3 compares the MD density profile to HM (left panel) and DIM (right panel) predictions. The initial equilibrium temperature T^0 is 0.72, in this case. Therefore, the low vapor density causes a correspondingly low condensation rate which only slightly perturbs the density profile in the liquid. The agreement of HM model density with MD is good, considering that, in the hybrid continuum-kinetic treatment of the flow, the interface has no structure. Hence, the liquid bulk extends up to the middle of the MD liquid-vapor interface, marked by the maximum of the modulus of the MD density gradient (dashed red line). The comparison of DIM density profile has to take into account that DIM considerably underestimates the condensation rate, for $T^0 = 0.72$. Hence, DIM interface position is behind MD one. To help comparing DIM and MD density profiles, a copy of the former has been translated to the right and superposed to the latter. DIM density in the liquid is slightly higher as compared to MD. This behavior is consistent with DIM temperature profile, shown in Fig. 4, which appears to be lower than the reference MD profile, both in the liquid and in the vapor. Also, DIM profile does not exhibit the interface temperature jump. produced by the MD simulation. The latter is well reproduced by HM, whose agreement with MD profile is good in both phases. The large discrepancy between DIM and MD velocity profiles (Fig. 5), in the vicinity of the liquid-vapor interface, is consistent with DIM underestimation of the condensation rate. On the contrary, the good HM estimate of condensation rate is confirmed by the good agreement of HM and MD velocity profiles in the va-

por (Fig. 5). As one might anticipate on the basis of Fig. 2c, at $T^0 = 0.9$ DIM flowfield description has considerably improved, whereas HM deviations from MD results are larger than in the lower temperature, described above.

Figure 6 compares the HM (left panel) and DIM (right panel) density profiles in the interface region. Both models match MD data well but HM density profile very slightly overestimates the liquid density. This result is in agreement with the slightly lower temperature profile in the liquid, obtained by HM, shown in Fig. 7b, whereas overall good agreement is obtained for the temperature profile in the vapor phase, as shown in Fig. 7a. The companion DIM temperature profiles, shown on the right panels of Fig. 7, show a slightly better agreement with MD in particular in the liquid region. At $T^0 = 0.9$, the observed HM and DIM deviations from MD condensation rate are more evident from the respective velocity profiles, rather than from the density and temperature profiles. As shown in Fig. 8, MD vapor macroscopic velocity in the z direction has higher average intensity than the corresponding quantity computed by DIM and HM. Both models underestimate the MD condensation rate but DIM discrepancy is smaller.

As anticipated by the comparisons of condensation rates (Fig. 2d), at $T^0 = 1.0$ DIM performs definitely better than the hybrid continuum-kinetic model which is based on a dilute vapor phase description. A strong discrepancy between MD and HM is observed in the liquid density profile and, to a lesser extent, in the vapor phase, next to the liquid vapor boundary (see Fig. 9). On the contrary, DIM density profile shows a very good agreement with MD data, in the vapor and liquid regions as well as in the interface (see Fig. 9). HM and DIM temperature profiles are shown in Fig. 10, on the left and right panel, respectively. As expected, HM higher liquid density profile reflects the lower liquid temperature observed in Fig. 10b. HM vapor temperature in the equilibrium region behind the reflected shock is also lower than the average value of MD simulation. At the right boundary of the z interval of Fig. 10a it is possible to spot the front of the HM shock already reflected by the advancing piston, because of the higher HM reflected shock velocity.

As it happens for density, DIM temperature profile is in very good agreement with MD profile. The comparisons are completed by showing HM and DIM velocity profiles in Fig. 11. It is seen that, for this temperature value, the behavior of HM and DIM is exchanged with respect to the results found for $T^0 = 0.72$. The smaller intensity of HM velocity explains why the condensation rate of the continuum-kinetic model is smaller than the reference value. On the other hand, the better agreement of DIM and MD velocity profiles explains why the continuum model, with its consistent description of the non-ideal LJ fluid, produces a better prediction of the reference

condensation rate.

V. CONCLUSIONS

The study described in the present paper is based on a small number of simulations of shock induced condensation flows, in conditions of increasing vapor non-ideality. The Lennard-Jones fluid has been simulated by three different computational methods, each reflecting a different description level of the same fluid. Although further simulations will be necessary to improve the accuracy and extend the number of studied cases, the available comparisons of MD reference simulations with the hybrid continuum-kinetic model (HM) results, based on a kinetic equation for a dilute vapor, shows that the latter provides a good description of condensation flow at the lowest temperature value considered in the study. HM results also show that unit condensation coefficient has to be assumed to match MD results. As the temperature of the unshocked vapor increases and the vapor non-ideality increases HM results deviate from reference, as expected. The fully continuum Diffuse Interface model (DIM) has the capability of handling both fluid phases by the same equations set. However, being based on Navier-Stokes-Fourier closures fails to describe kinetic effects. As expected, DIM deviates from MD results at low temperature when kinetic effects are stronger. However, as temperature increases, it is expected that the Knudsen layer, close to liquid-vapor interface, gradually disappears. Actually, the obtained results indicate that DIM description becomes more accurate as the vapor non-ideality increases. The obtained results indicate that there exist a range of flow conditions where the vapor phase is not ideal enough to guarantee the validity of a traditional kinetic description that neglects vapor non-ideality and not dense enough for a hydrodynamic description that includes vapor non-ideality but neglects kinetic effects.

The attempt to include kinetic effects into non-ideal fluid has to face the problem of a limited development of the kinetic theory of dense gases[39]. A possible way to give DIM the capability to include the description of kinetic layers is to extend moments methods developed for the Boltzmann Equation[40] to kinetic models for liquid-vapor systems out of equilibrium[10–12,14]. Although preliminary work along this research line has been done[41], the complexity of equations require further developments.

VI. ACKNOWLEDGEMENTS

This paper is dedicated to the memory of Professor Jason Reese, whose enthusiasm and scientific contributions will not be forgotten.

VII. DATA AVAILABILITY

The data that support the findings of this study are available from the corresponding author upon reasonable request.

REFERENCES

[1]P. Barbante and A. Frezzotti, "Simulations of condensation flows induced by reflection of weak shocks from liquid surfaces," AIP Conference Proceedings **1786** (2016).

[2]M. Marek and J. Straub, "Analysis of the evaporation coefficient and evaporation coefficient of water," Int.J. Heat and Mass Transf. **44**, 39–53 (2001).

[3]A. Persad and C. Ward, "Expressions for the evaporation and condensation coefficients in the Hertz-Knudsen relation," Chemical Reviews **116**, 7727–7767 (2016).

[4]S. S. Sazhin, "Advanced models of fuel droplet heating and evaporation," Prog. Energ. Combust. **32**, 162–214 (2006).

[5]M. Shusser, T. Ytrehus, and D. Weihs, "Kinetic theory analysis of explosive boiling of a liquid droplet," Fluid. Dyn. Res. **27**, 353–365 (2000).

[6]T. Ytrehus, "Molecular-flow effects in evaporation and condensation at interfaces," Multiphase Science and Technology **9**, 205–327 (1997).

[7]Y. Sone, "Kinetic theoretical studies of the half-space problem of evaporation and condensation," TTSP **29**, 227–260 (2000).

[8]A. Frezzotti, P. Barbante, and L. Gibelli, "Direct simulation monte carlo applications to liquid-vapor flows," Physics of Fluids **31** (2019).

[9]K. Ohashi, K. Kobayashi, H. Fujii, and M. Watanabe, "Evaporation coefficient and condensation coefficient of vapor under high gas pressure conditions," Scientific Reports **10** (2020).

[10]L. de Sobrino, "On the kinetic theory of a Van der Waals gas," Can. J. Phys. **45**, 363–385 (1967).

[11]M. Grmela, "Kinetic equation approach to phase transitions," Journal of Statistical Physics **3**, 347 (1971).

[12]A. Frezzotti, L. Gibelli, and S. Lorenzani, "Mean field kinetic theory description of evaporation of a fluid into vacuum," Phys. Fluids **17**, 012102 (2005).

[13]M. Kon, K. Kobayashi, and M. Watanabe, "Method of determining kinetic boundary conditions in net evaporation/condensation," Physics of Fluids **26** (2014).

[14]E. S. Benilov and M. S. Benilov, "Energy conservation and H theorem for the Enskog-Vlasov equation," Phys. Rev. E **97**, 062115 (2018).

[15]J.-P. Hansen and I. McDonald, *Theory of Simple Liquids* (Academic Press, London, UK, 2006).

[16]S. Fujikawa, M. Okuda, T. Akamatsu, and T. Goto, "Non-equilibrium vapour condensation on a shock-tube endwall behind a reflected shock wave," Journal of Fluid Mechanics **183**, 293–324.

[17]S. Fujikawa, T. Yano, and M. Watanabe, *Vapor-Liquid Interfaces, Bubbles and Droplets* (Springer, 2011).

[18]M. Allen and D. Tildesley, *Computer Simulation of Liquids* (Clarendon Press, Oxford, 1987).

[19]D. M. Anderson, G. B. McFadden, and A. A. Wheeler, "Diffuse-Interface Methods in Fluid Mechanics," Annu. Rev. Fluid Mech. **30**, 139–165 (1998).

[20]C. Cercignani, *The Boltzmann Equation and Its Applications* (Springer-Verlag, Berlin, 1988).

[21]P. Barbante and A. Frezzotti, "A comparison of models for the evaporation of the Lennard-Jones fluid," European Journal of Mechanics - B/Fluids **64**, 69 – 80 (2017).

[22]Aldo Frezzotti and Tor Ytrehus, "Kinetic theory study of steady condensation of a polyatomic gas," Physics of Fluids **18**, 027101 (2006).

[23]A. Frezzotti, "Boundary conditions at the vapor-liquid interface," Physics of Fluids **23**, 030609 (2011).

[24]J. K. Johnson, J. A. Zollweg, and K. E. Gubbins, "The Lennard-Jones equation of state revisited," Molecular Physics **78**, 591–618 (1993).

[25]G. Galliero, C. Boned, and A. Baylaucq, "Molecular Dynamics Study of the Lennard-Jones Fluid Viscosity: Application to Real Fluids," Ind. Eng. Chem. Res. **44**, 6963–6972 (2005).

[26]M. Bugel and G. Galliero, "Thermal Conductivity of the Lennard-Jones Fluid: an Empirical Correlation," Chemical Physics **352**, 249–257 (2008).

[27]G. Galliero, "Lennard-Jones fluid-fluid interfaces under shear," Phys. Rev. E **81**, 056306 (2010).

[28]S. Chapman and T. G. Cowling, *The Mathematical Theory of Non-Uniform Gases* (Cambridge University Press, Cambridge UK, 1990).

[29]L. D. Landau and E. M. Lifshitz, *Fluid Mechanics*, 2nd ed., Course of Theoretical Physics No. 6 (Butterworth-Heinemann, 1987).

[30]A. Frezzotti, "Non-equilibrium structure of the vapor-liquid interface of a binary fluid," in *27th International Symposium on Rarefied Gas Dynamics*, AIP Conference Proceedings, Vol. 1333, edited by D. A. Levin, I. J. Wysong, and A. L. Garcia (AIP, 2011) pp. 161–166.

[31]M. Allen and D. Tildesley, *Computer Simulation of Liquids* (Clarendon Press, 1989).

[32]D. J. Korteweg, "Sur la forme que prendent les équations du mouvements des fluides si l'on tien compte des forces capillaires causées par des variations de densité considérables mais continues et sur la théorie de la capillarité dans l'hypothèse d'une variation continue de la densité," Arch. Néerl. Sci. Exactes Nat. Ser. II **6**, 1–24 (1901).

[33]J. Dunn and J. Serrin, "On the thermomechanics of interstitial working," Archive for Rational Mechanics and Analysis **88**, 95–133 (1985).

[34]A. Frezzotti, "Kinetic theory description of the evaporation of multi-component substances," in *Rarefied Gas Dynamics, Proceedings of the 20th International Symposium, 19-23 August 1996, Beijing, China*, edited by C. Shen (Peking University Press, Beijing, China, 1997) pp. 837–846.

[35]G. A. Bird, *Molecular Gas Dynamics and the Direct Simulation of Gas Flows* (Clarendon Press, Oxford, 1994) .

[36]T. Ishiyama, S. Fujikawa, T. Kurz, and W. Lauterborn, "Nonequilibrium kinetic boundary condition at the vapor-liquid interface of argon," Physical Review E **88**, 042406. (2013).

[37]A. Tokunaga and T. Tsuruta, "Nonequilibrium molecular dynamics study on energy accommodation coefficient on condensing liquid surface molecular boundary conditions for heat and mass transfer," Physics of Fluids **32**, 112011 (2020), https://doi.org/10.1063/5.0027945.

[38]S. Busuioc, L. Gibelli, D. A. Lockerby, and J. E. Sprittles, "Velocity distribution function of spontaneously evaporating atoms," Phys. Rev. Fluids **5**, 103401 (2020) .

[39]P. Resibois and M. DeLeener, *Classical kinetic theory of fluids* (J. Wiley & Sons, New York, 1977).

[40]A. Rana and H. Struchtrup, "Thermodynamically admissible boundary conditions for the regularized 13 moment equations," Physics of Fluids **28**, 027105 (2016).

[41]H. Struchtrup and A. Frezzotti, "Grad's 13 moments approximation for Enskog-Vlasov equation," AIP Conference Proceedings **2132** (2019).

Figures and captions

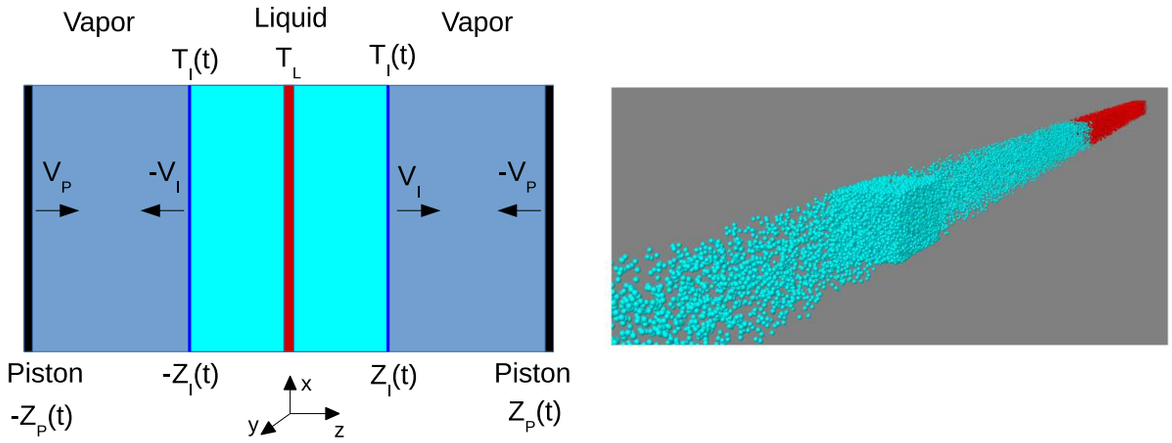

FIG. 1. **Left panel**: Schematic representation of MD simulation domain and setup. The central red strip indicates the central thermostatted liquid slice. Spatial scales are arbitrary.

Right panel: Snapshot of atoms positions within the MD shock tube, at time $t = 1600$ of a MD simulation with $T^0 = 0.9$ and $V_p = 0.2$. The central region of the picture shows the roughly parallelepipedal liquid column, whereas the upper right region shows the shocked vapor, whose atoms are marked by red color.

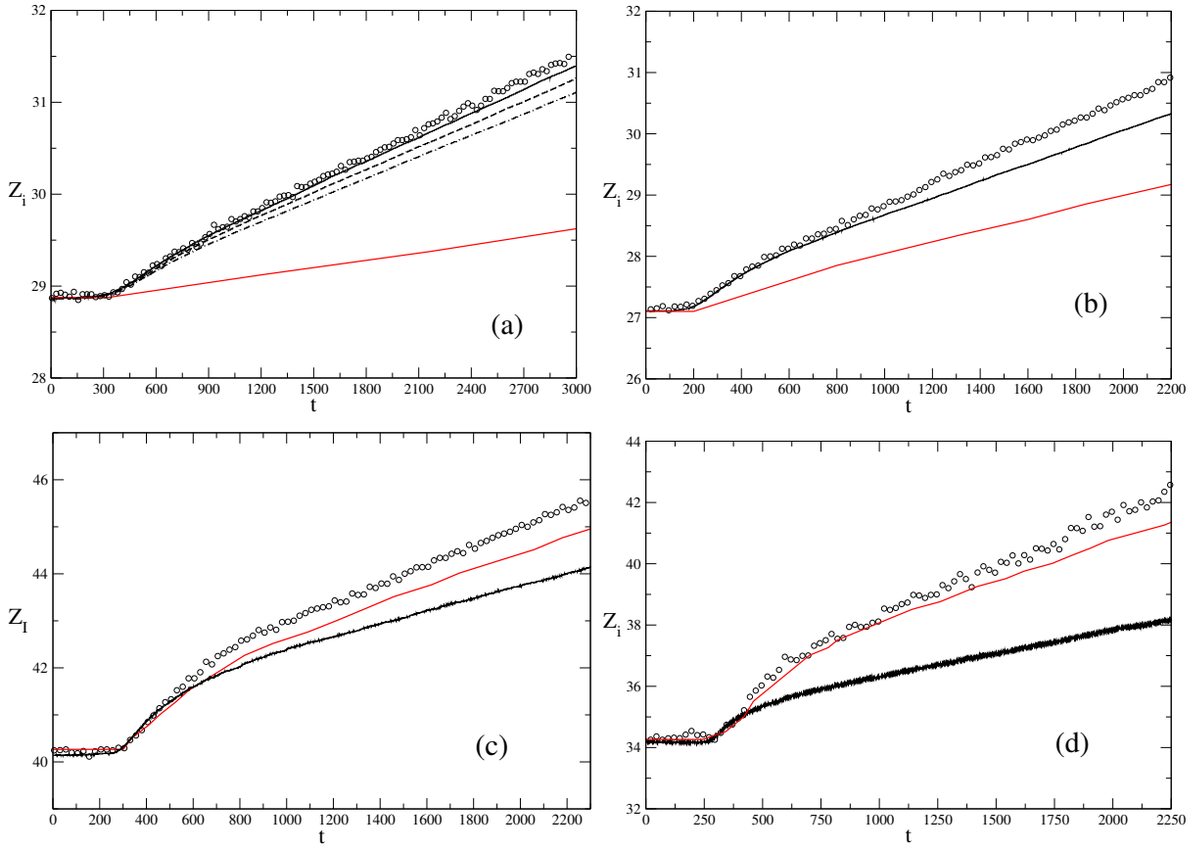

FIG. 2. Comparisons of MD, DIM and HM time histories of interface position during condensation. In all panels ○: MD; Black solid lines: HM, $\sigma_c = 1.0$; Red solid lines DIM. **(a)** - $T^0 = 0.72, V_p = 0.2$, dashed line: $\sigma_c = 0.9$, dot-dashed line: $\sigma_c = 0.8$; **(b)** - $T^0 = 0.8, V_p = 0.2$; **(c)** - $T^0 = 0.9, V_p = 0.2$; **(d)** - $T^0 = 1.0, V_p = 0.2$.

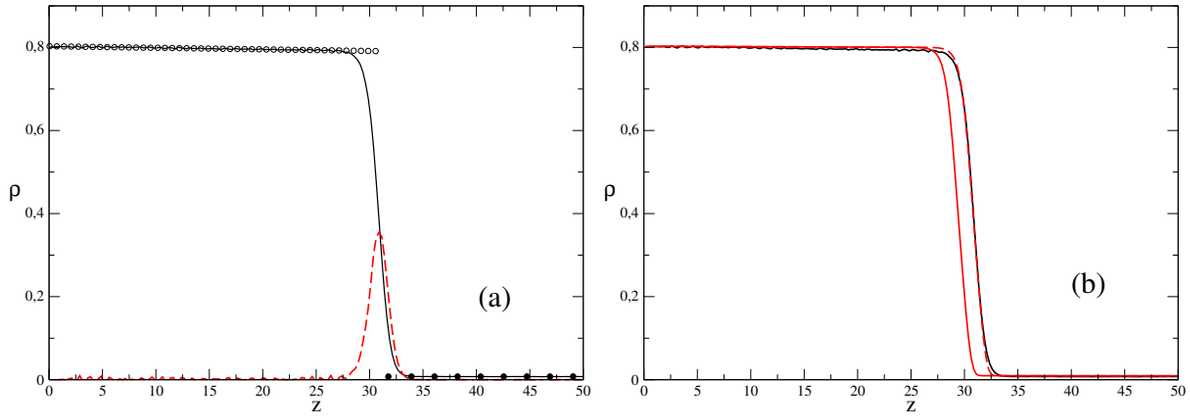

FIG. 3. Comparisons of MD, DIM and HM density profiles during condensation. $T^0 = 0.72, V_p = 0.2$. **(a)** - Solid black line: MD density profile; red dashed line: modulus of MD density gradient; ○: HM density profile in the liquid; ●: HM density profile in the vapor. **(b)** - Solid black line: MD density profile; red solid line: DIM density profile; red dashed line: shifted DIM density profile.

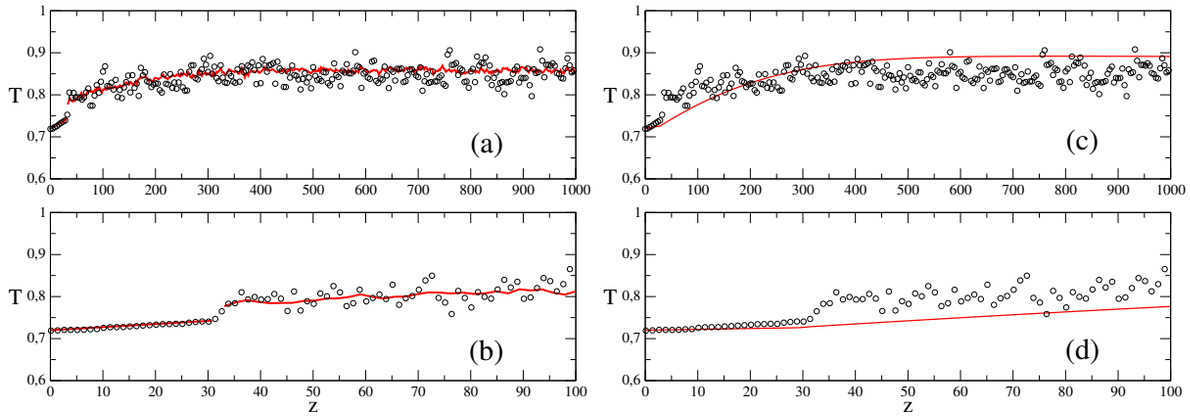

FIG. 4. Comparisons of MD, DIM and HM temperature profiles during condensation. $T^0 = 0.72, V_p = 0.2$. **(a)** - ○ MD temperature profile; solid red line: HM temperature profiles in liquid and vapor phase. **(b)** - Enlarged view of MD and HM temperature profiles in the interface region. **(c)** - ○ MD temperature profile; solid red line: DIM temperature profiles in liquid and vapor phase. **(d)** - Enlarged view of MD and DIM temperature profiles in the interface region.

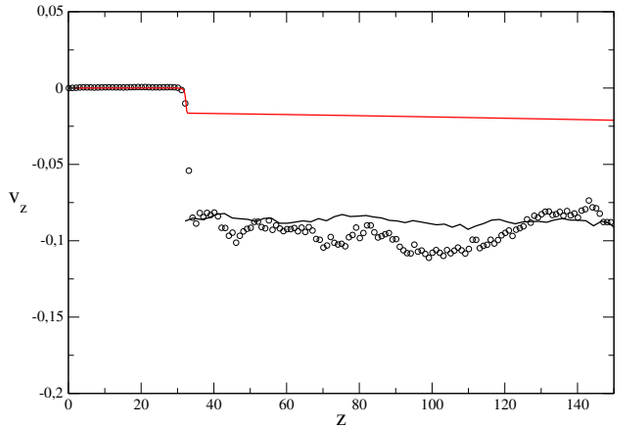

FIG. 5. Comparisons of MD, DIM and HM velocity profiles during condensation, $T^0 = 0.72, V_p = 0.2$. $\circ$ MD: velocity profile; Solid black line: HM velocity profile in the vapor; Solid red line: DIM velocity profile.

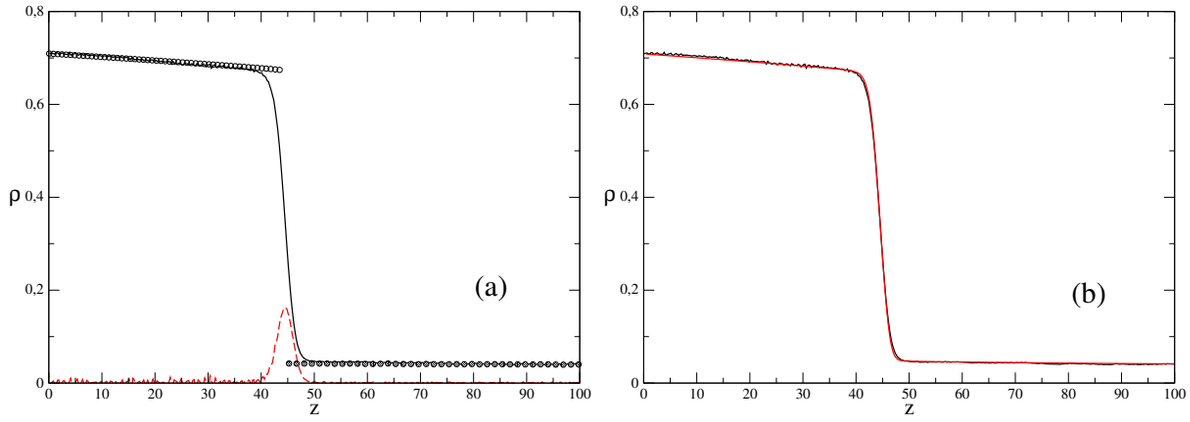

FIG. 6. Comparisons of MD, DIM and HM density profiles during condensation. $T^0 = 0.9, V_p = 0.2$. **(a)** - Solid black line: MD density profile; red dashed line: modulus of MD density gradient; ○: HM density profile in the liquid; ●: HM density profile in the vapor. **(b)** - Solid black line: MD density profile; red solid line: DIM density profile.

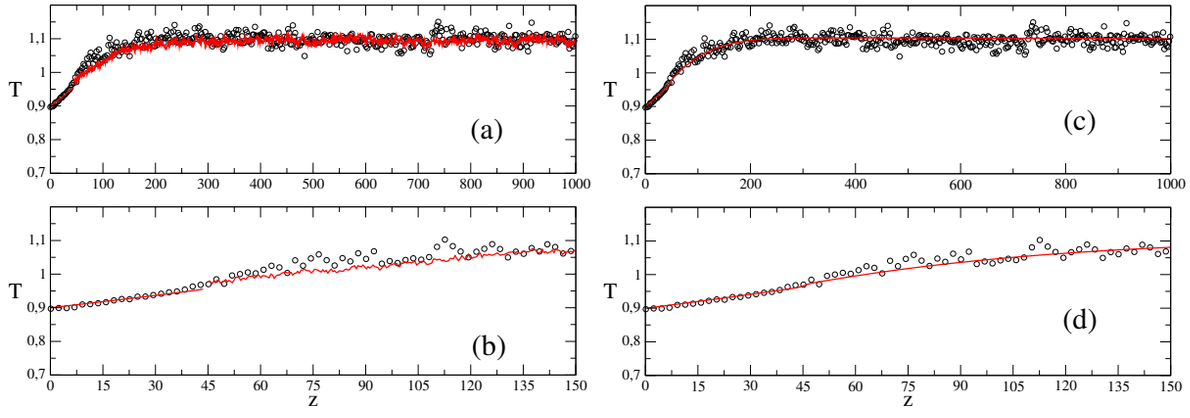

FIG. 7. Comparisons of MD, DIM and HM temperature profiles during condensation. $T^0 = 0.9, V_p = 0.2$. **(a)** - ○ MD temperature profile; solid red line: HM temperature profiles in liquid and vapor phase. **(b)** - Enlarged view of MD and HM temperature profiles in the interface region. **(c)** - ○ MD temperature profile; solid red line: DIM temperature profiles in liquid and vapor phase. **(d)** - Enlarged view of MD and DIM temperature profiles in the interface region.

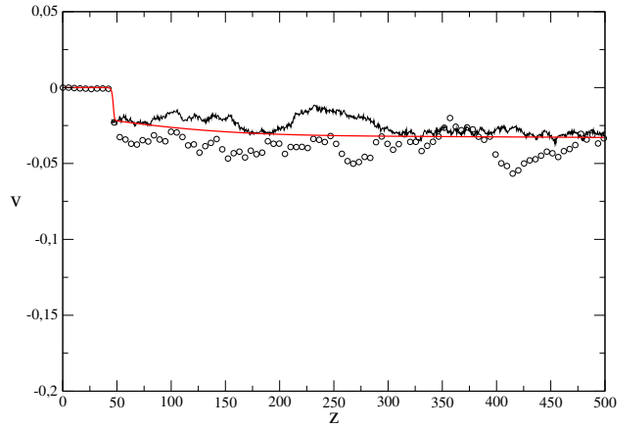

FIG. 8. Comparisons of MD, DIM and HM velocity profiles during condensation, $T^0 = 0.9, V_p = 0.2$. $\circ$ MD: velocity profile; Solid black line: HM velocity profile in the vapor; Solid red line: DIM velocity profile.

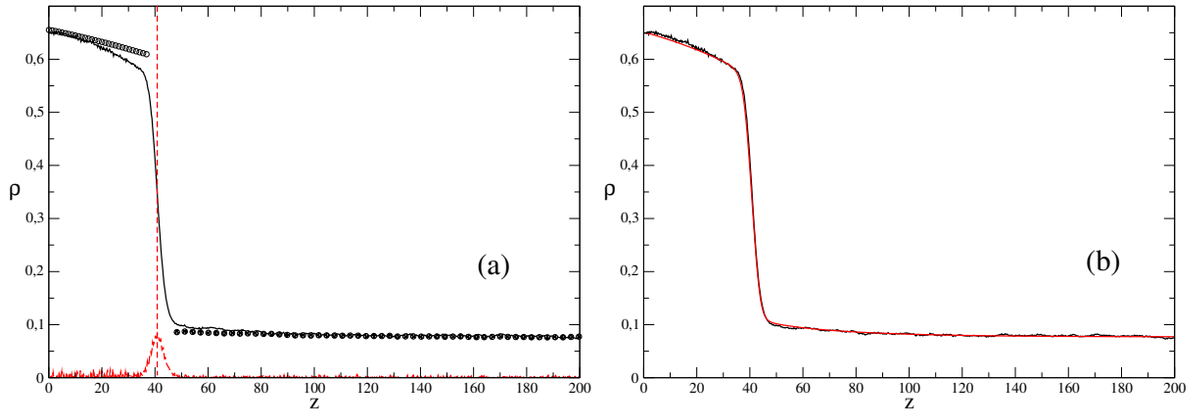

FIG. 9. Comparisons of MD, DIM and HM density profiles during condensation. $T^0 = 1.0, V_p = 0.2$. **(a)** - Solid black line: MD density profile; red dashed line: modulus of MD density gradient; ○: HM density profile in the liquid; ●: HM density profile in the vapor. **(b)** - Solid black line: MD density profile; red solid line: DIM density profile.

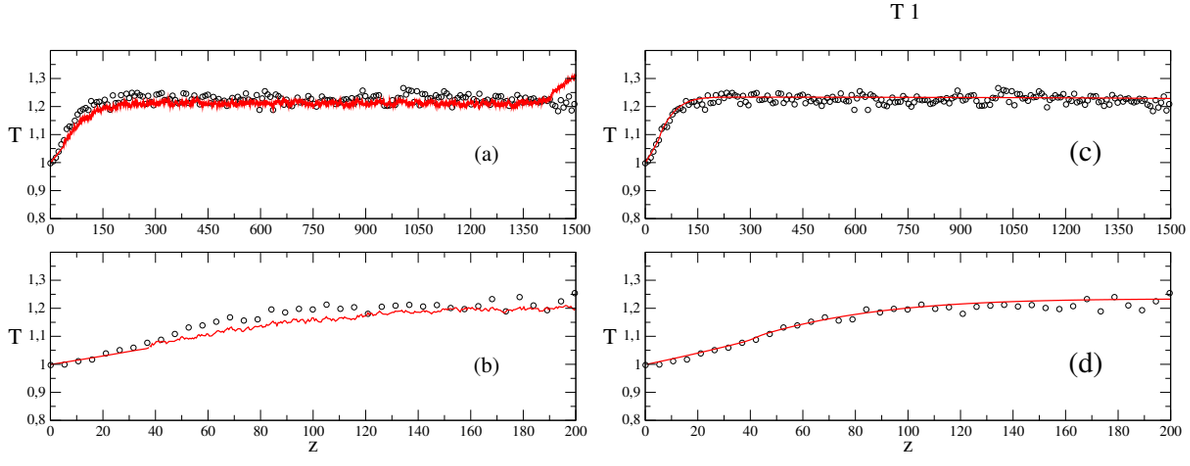

FIG. 10. Comparisons of MD, DIM and HM temperature profiles during condensation. $T^0 = 1.0, V_p = 0.2$. **(a)** - ○ MD temperature profile; solid red line: HM temperature profiles in liquid and vapor phase. **(b)** - Enlarged view of MD and HM temperature profiles in the interface region. **(c)** - ○ MD temperature profile; solid red line: DIM temperature profiles in liquid and vapor phase. **(d)** - Enlarged view of MD and DIM temperature profiles in the interface region.

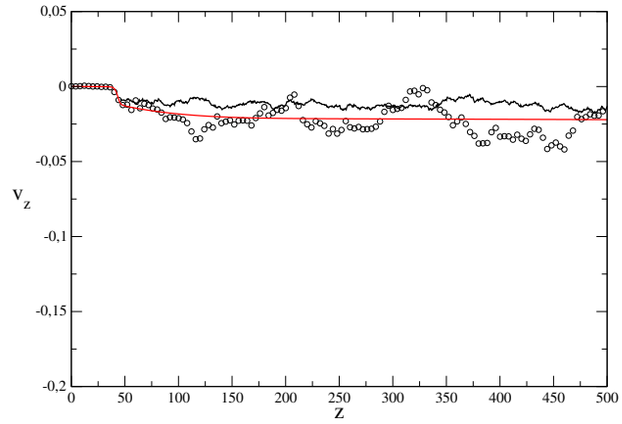

FIG. 11. Comparisons of MD, DIM and HM velocity profiles during condensation, $T^0 = 1.0, V_p = 0.2$. $\circ$ MD: velocity profile; Solid black line: HM velocity profile in the vapor; Solid red line: DIM velocity profile.

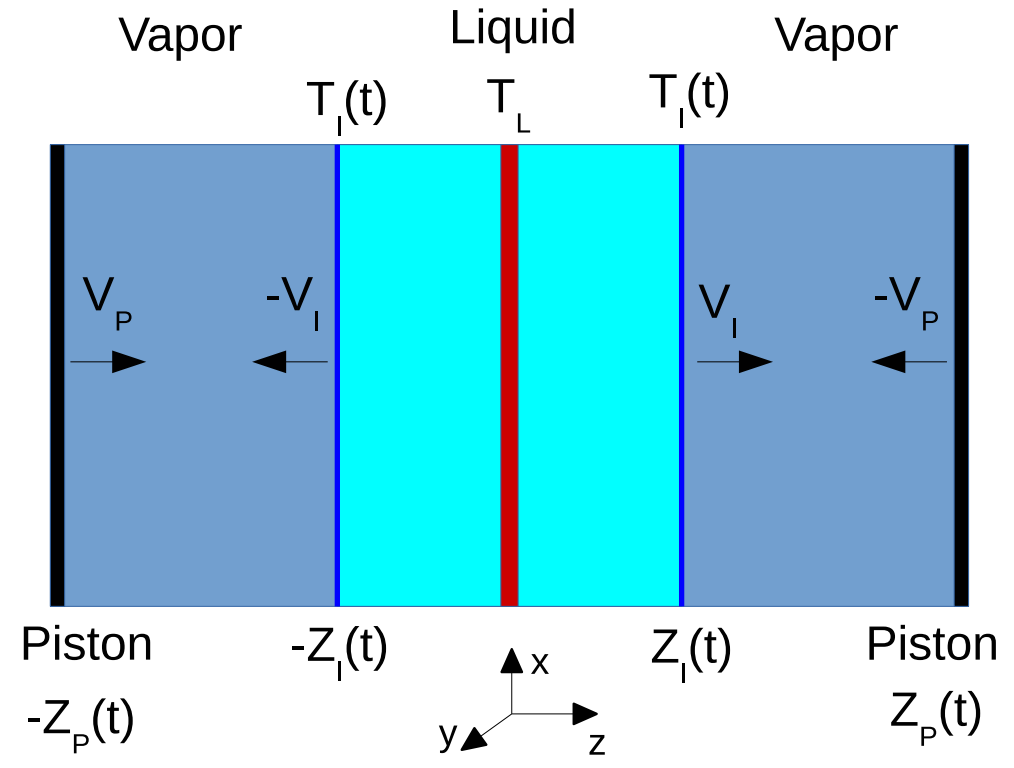
Vapor
Liquid
Vapor
$T_I(t)$
T_L
$T_I(t)$
V_P
$-V_I$
V_I
$-V_P$
Piston
$-Z_P(t)$
$-Z_I(t)$
$Z_I(t)$
Piston
$Z_P(t)$
x
y
z

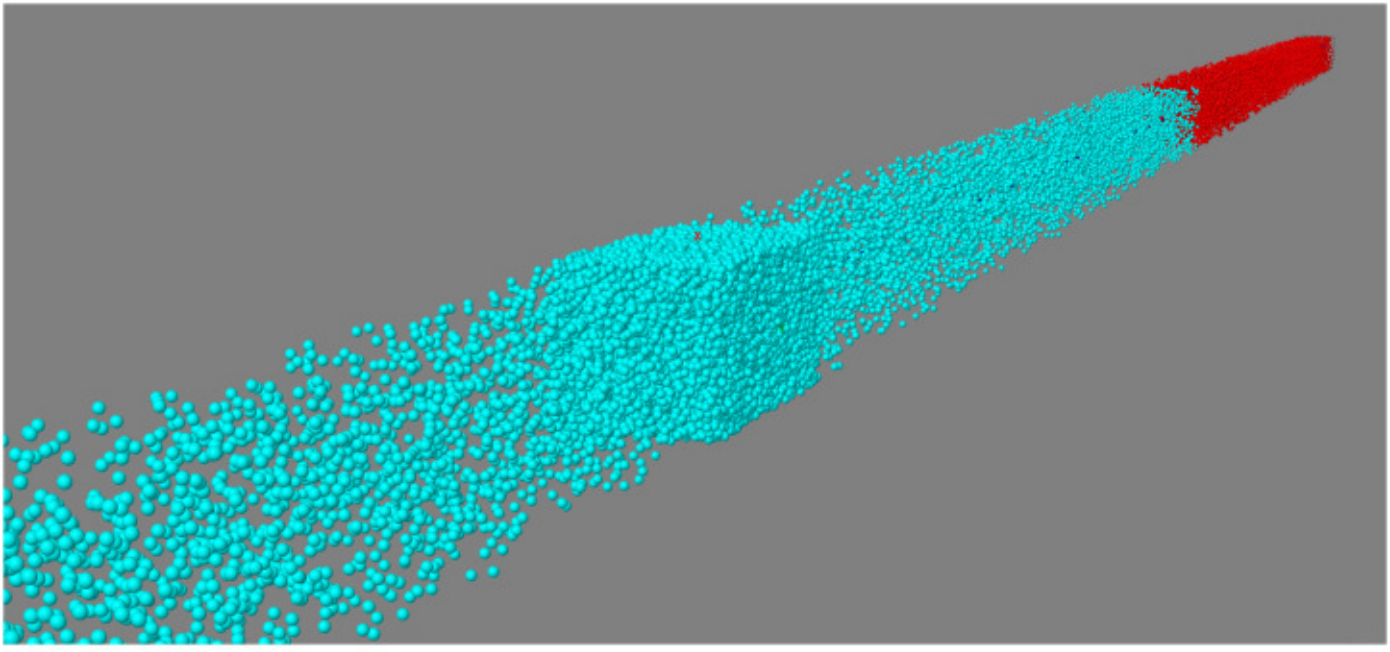

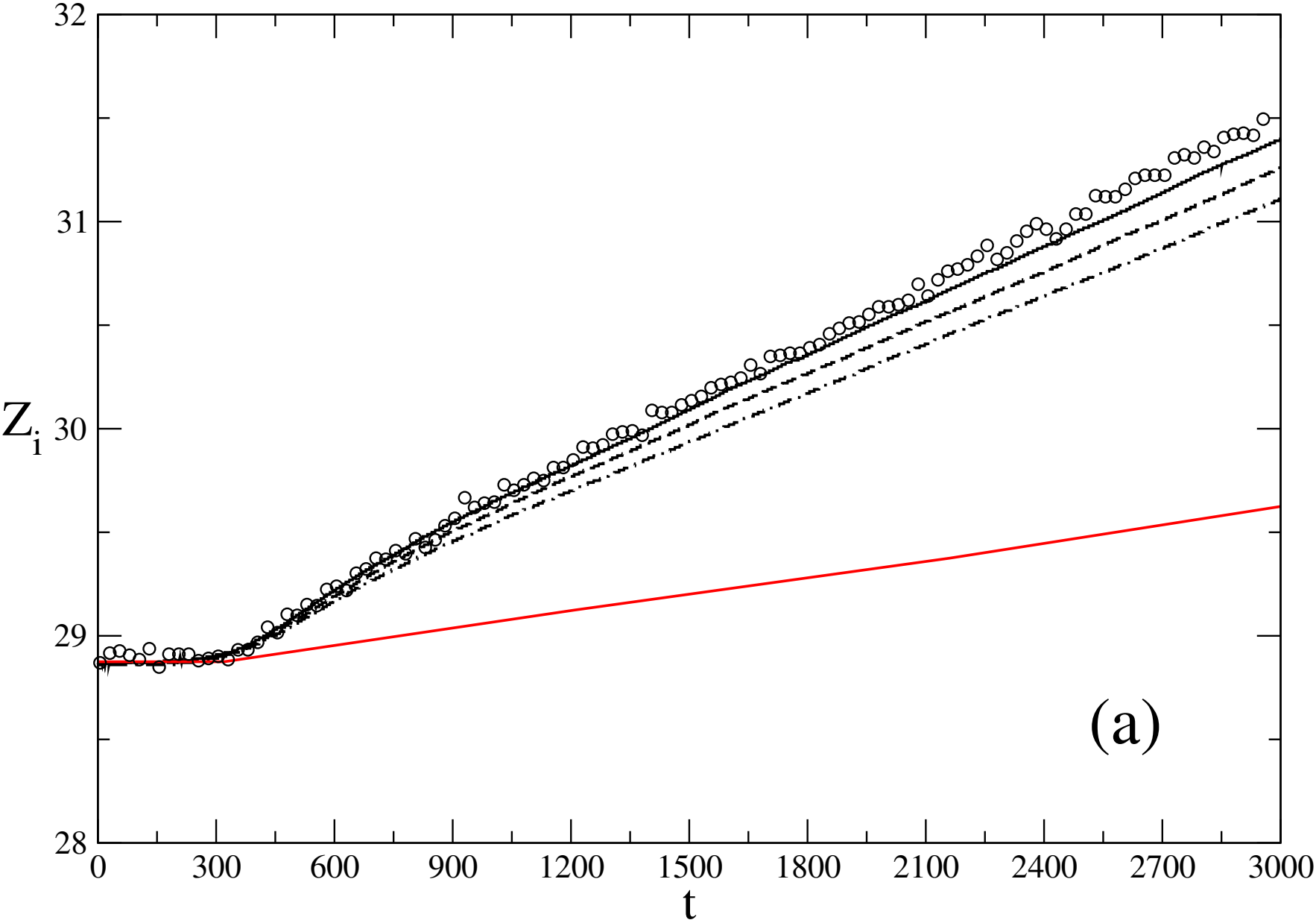
32
31
30
29
28
Z_i
0
300
600
900
1200
1500
1800
2100
2400
2700
3000
t
(a)

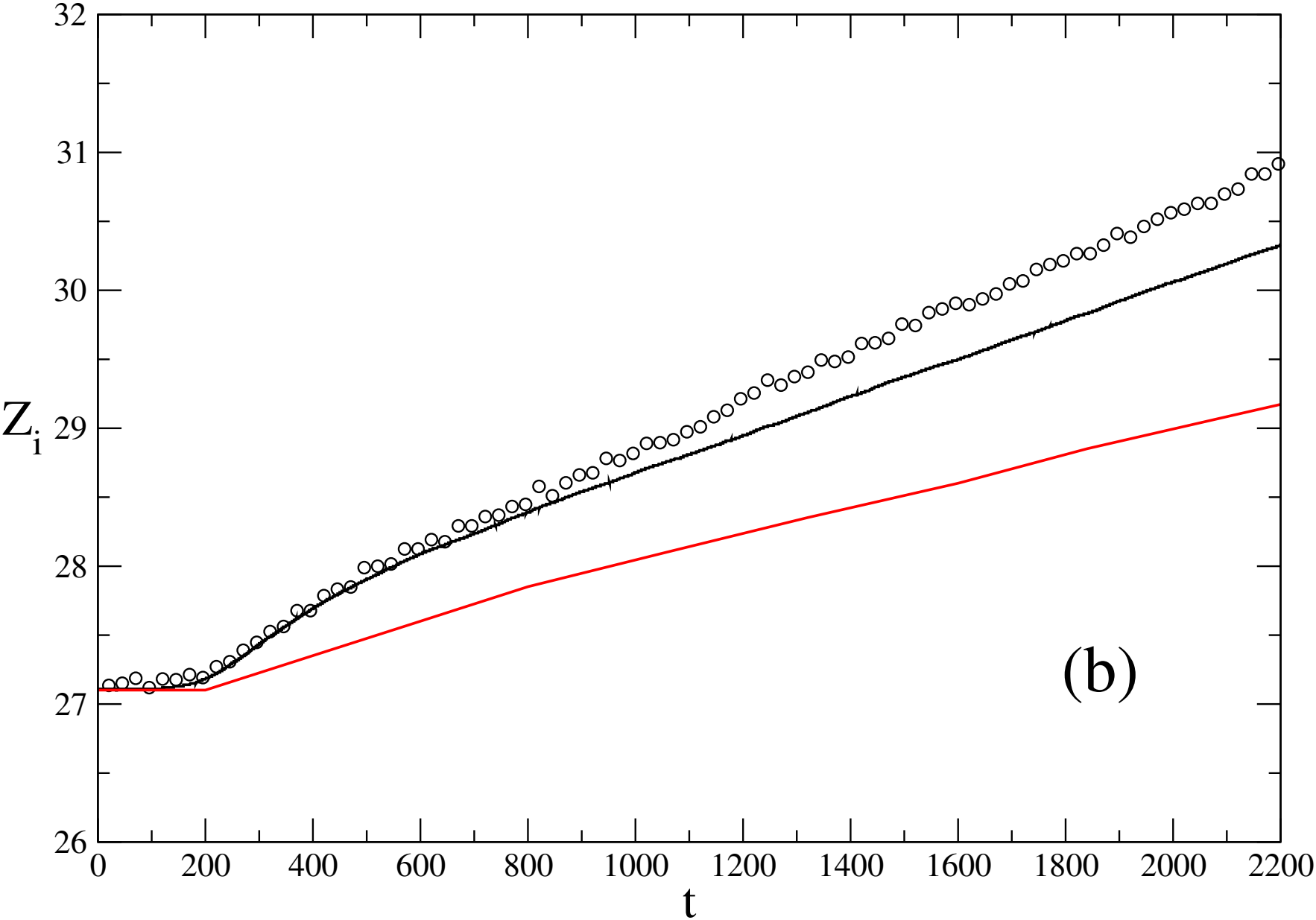
32
31
30
29
28
27
26
Z_i
0
200
400
600
800
1000
1200
1400
1600
1800
2000
2200
t
(b)

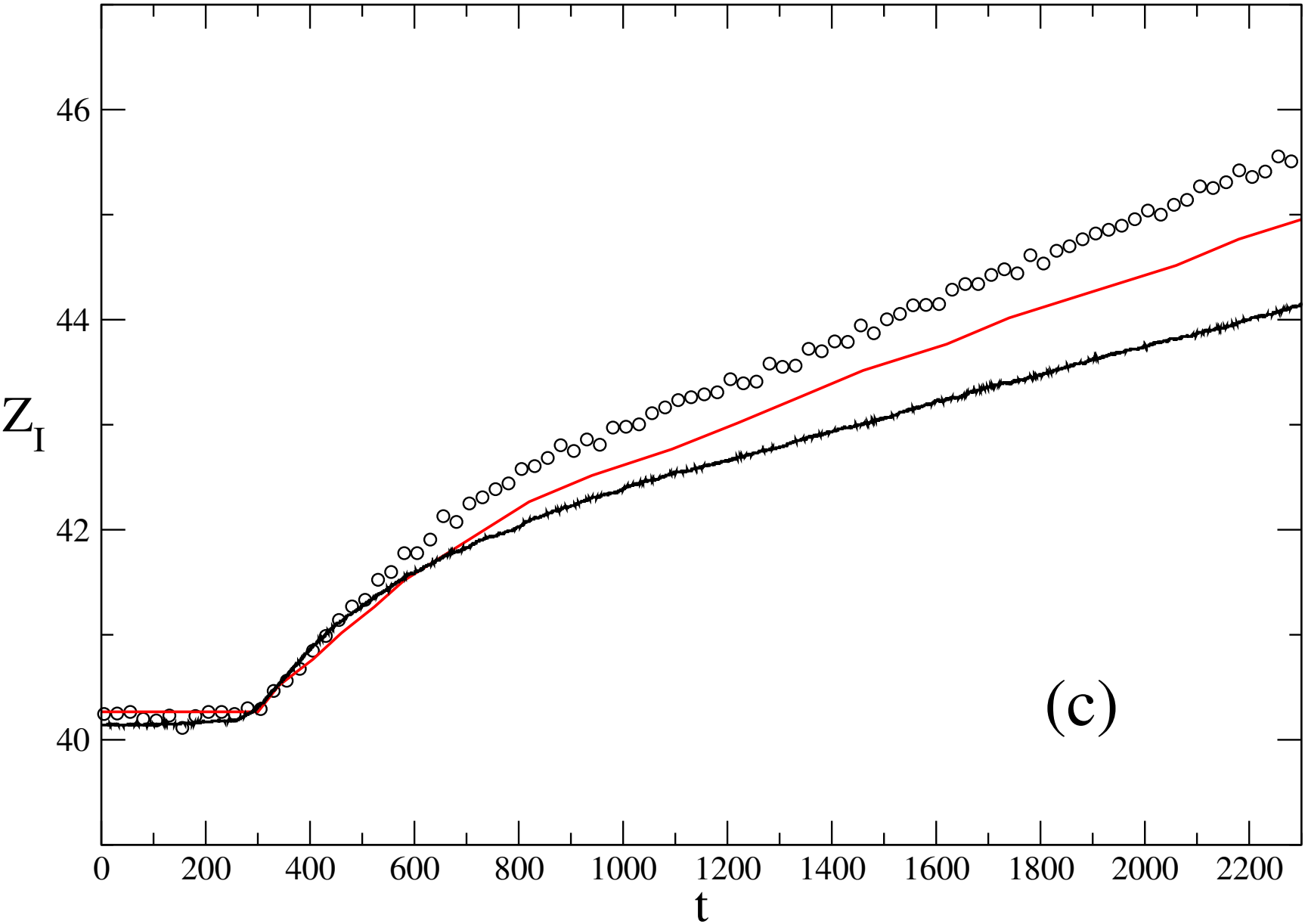
46
44
42
40
Z_I
0
200
400
600
800
1000
1200
1400
1600
1800
2000
2200
t
(c)

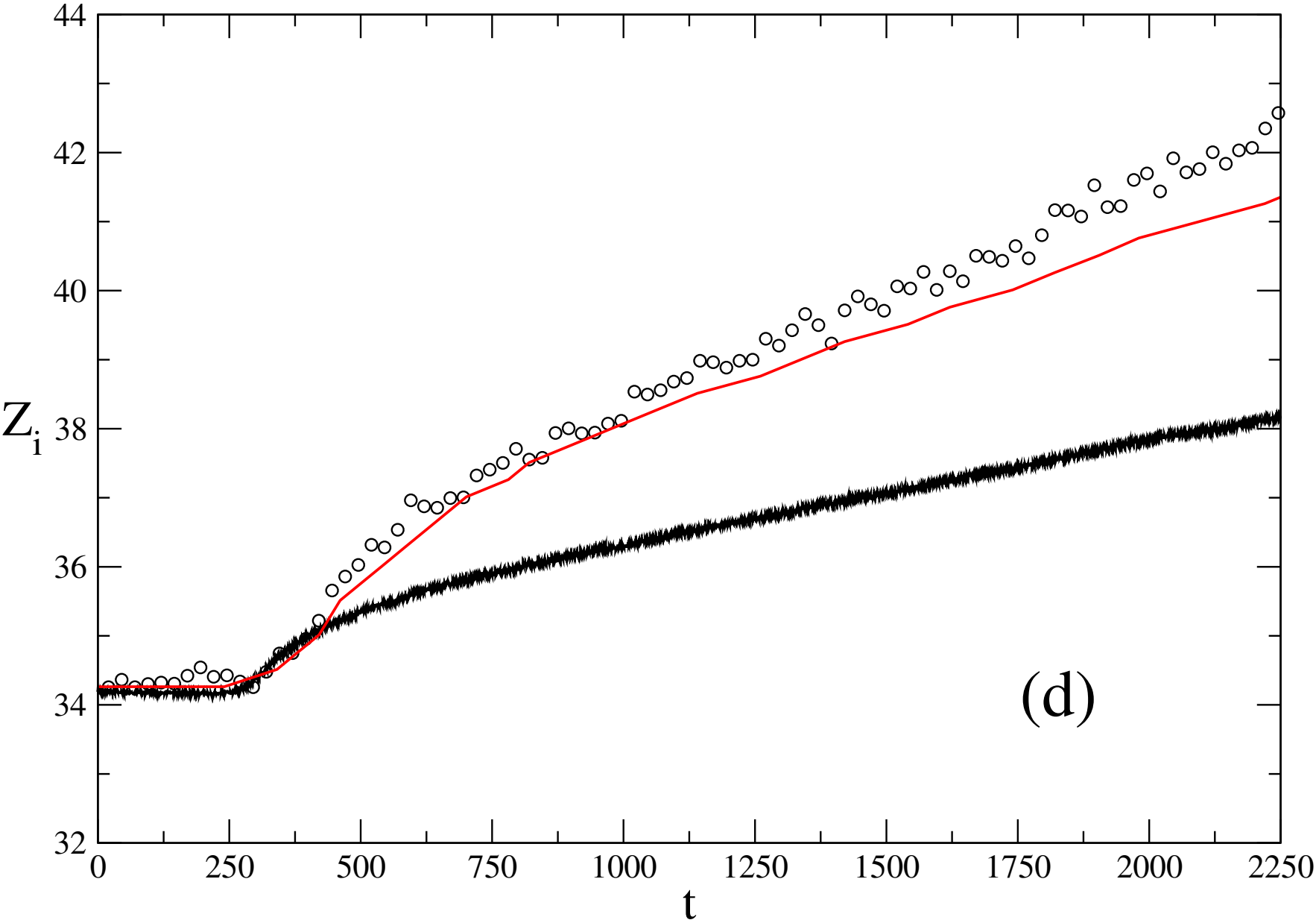
44
42
40
38
36
34
32
Z_i
0
250
500
750
1000
1250
1500
1750
2000
2250
t
(d)

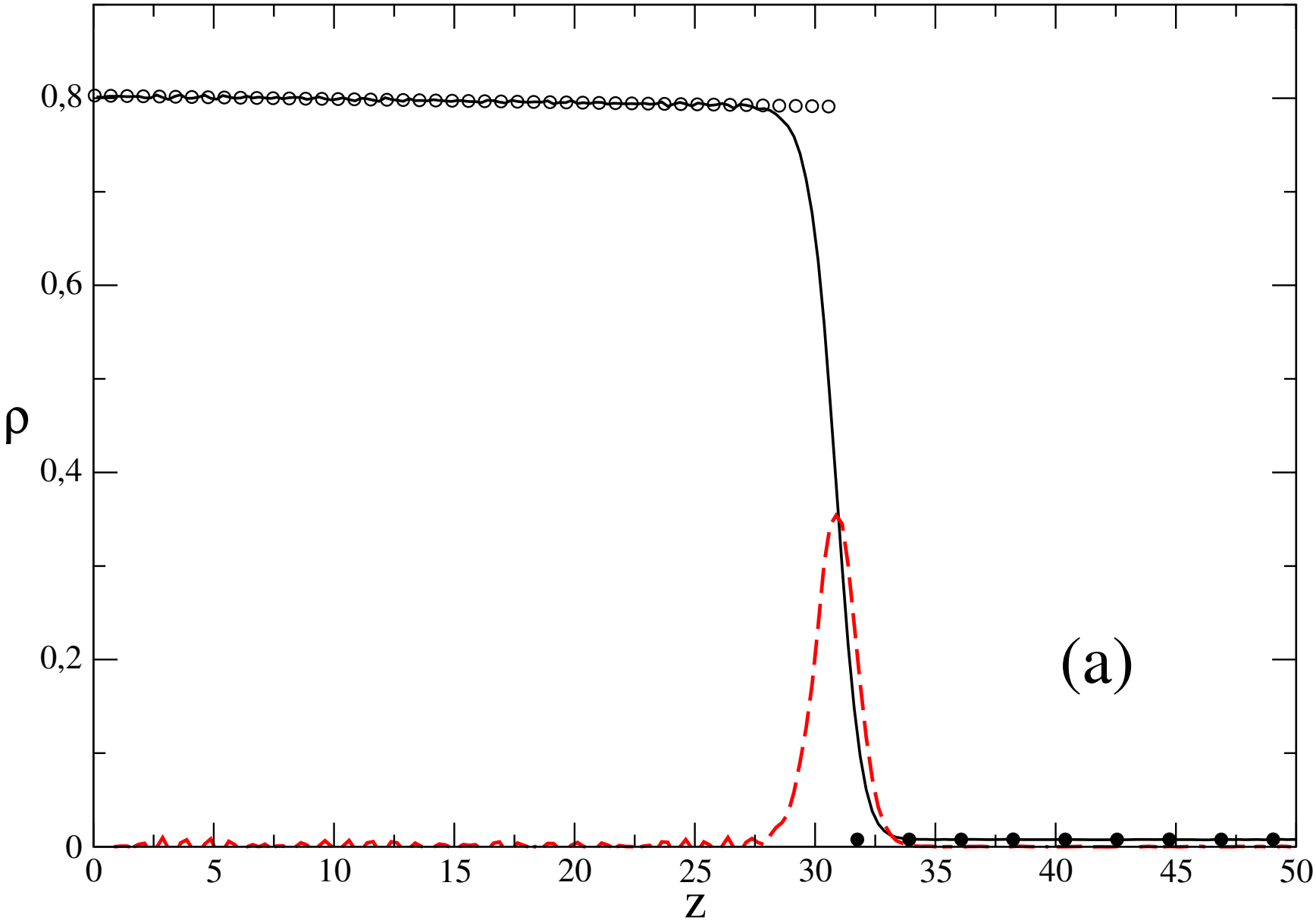
0,8
0,6
0,4
0,2
0
ρ
0
5
10
15
20
25
30
35
40
45
50
z
(a)

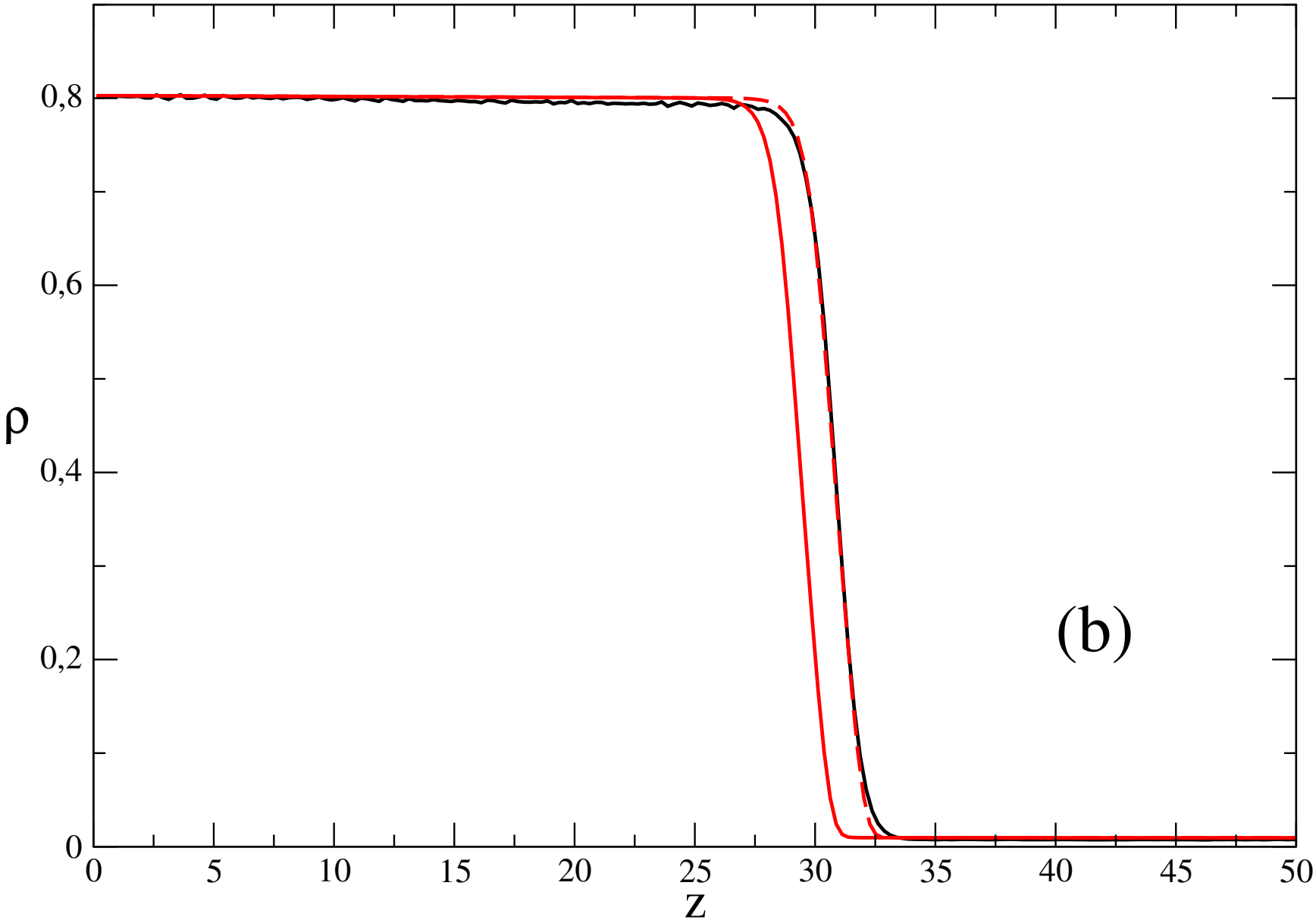
0,8
0,6
0,4
0,2
0
ρ
0
5
10
15
20
25
30
35
40
45
50
z
(b)

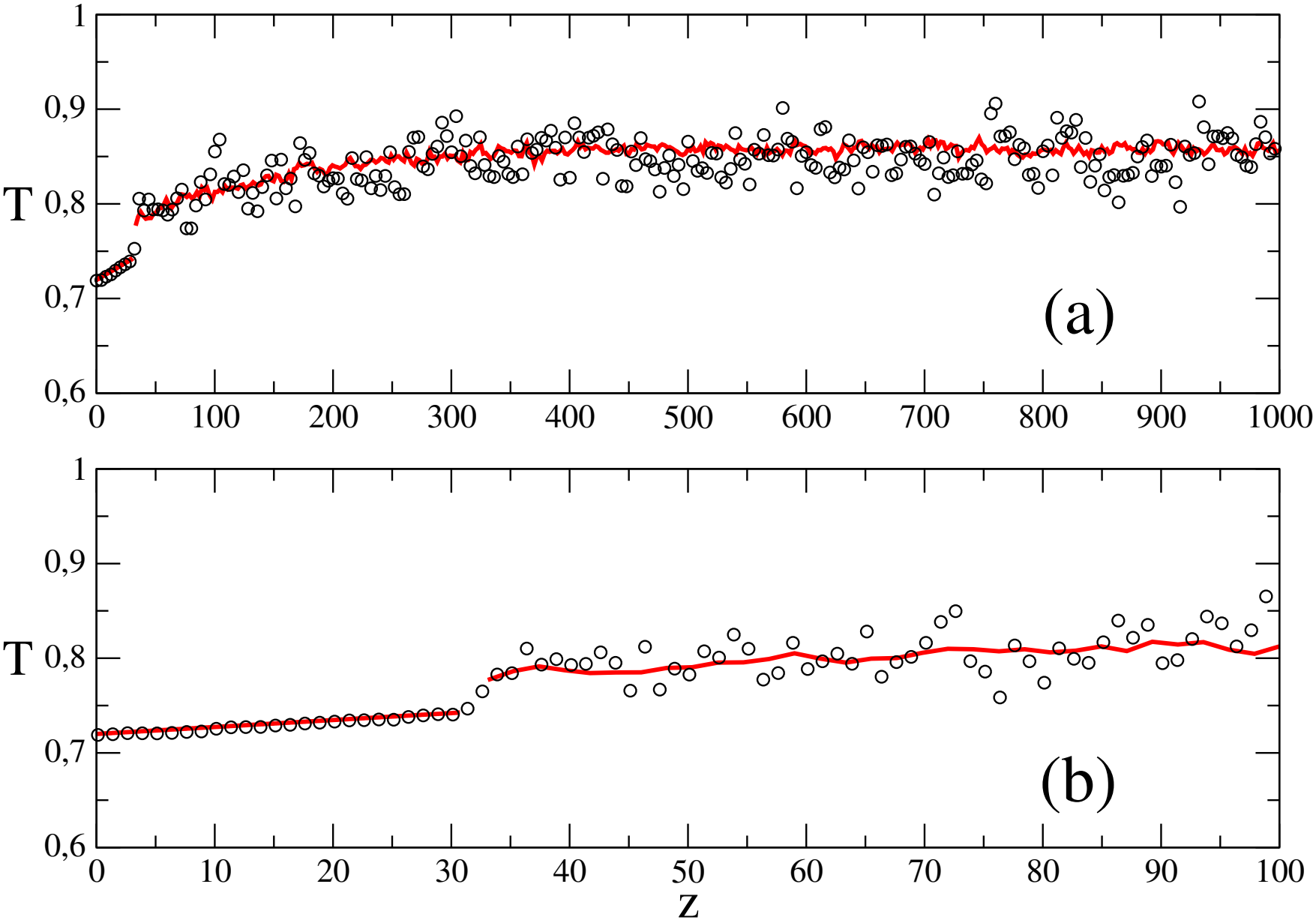
T
1
0,9
0,8
0,7
0,6
0
100
200
300
400
500
600
700
800
900
1000
(a)
T
1
0,9
0,8
0,7
0,6
0
10
20
30
40
50
60
70
80
90
100
z
(b)

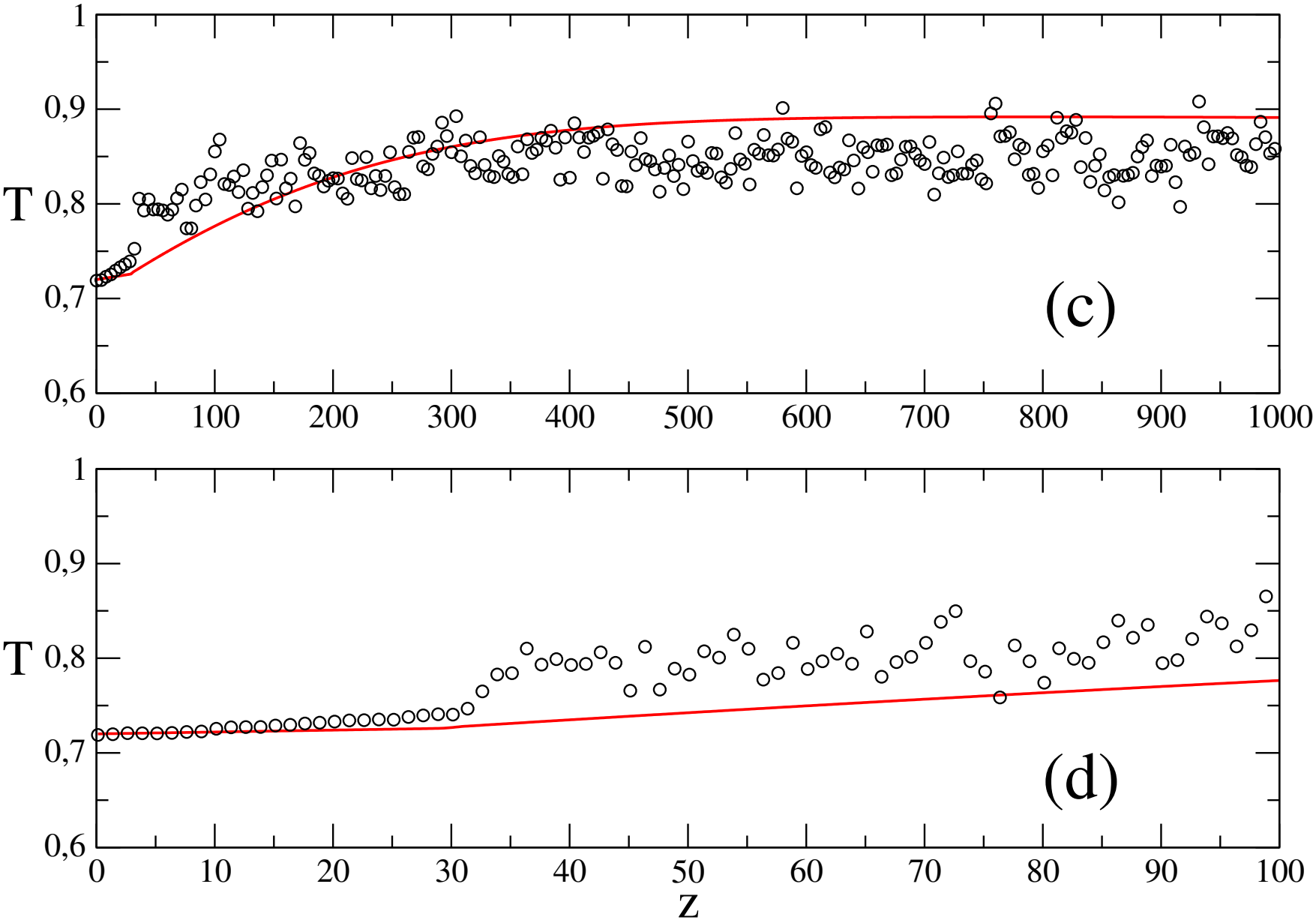
T
1
0,9
0,8
0,7
0,6
0
100
200
300
400
500
600
700
800
900
1000
(c)
T
1
0,9
0,8
0,7
0,6
0
10
20
30
40
50
60
70
80
90
100
z
(d)

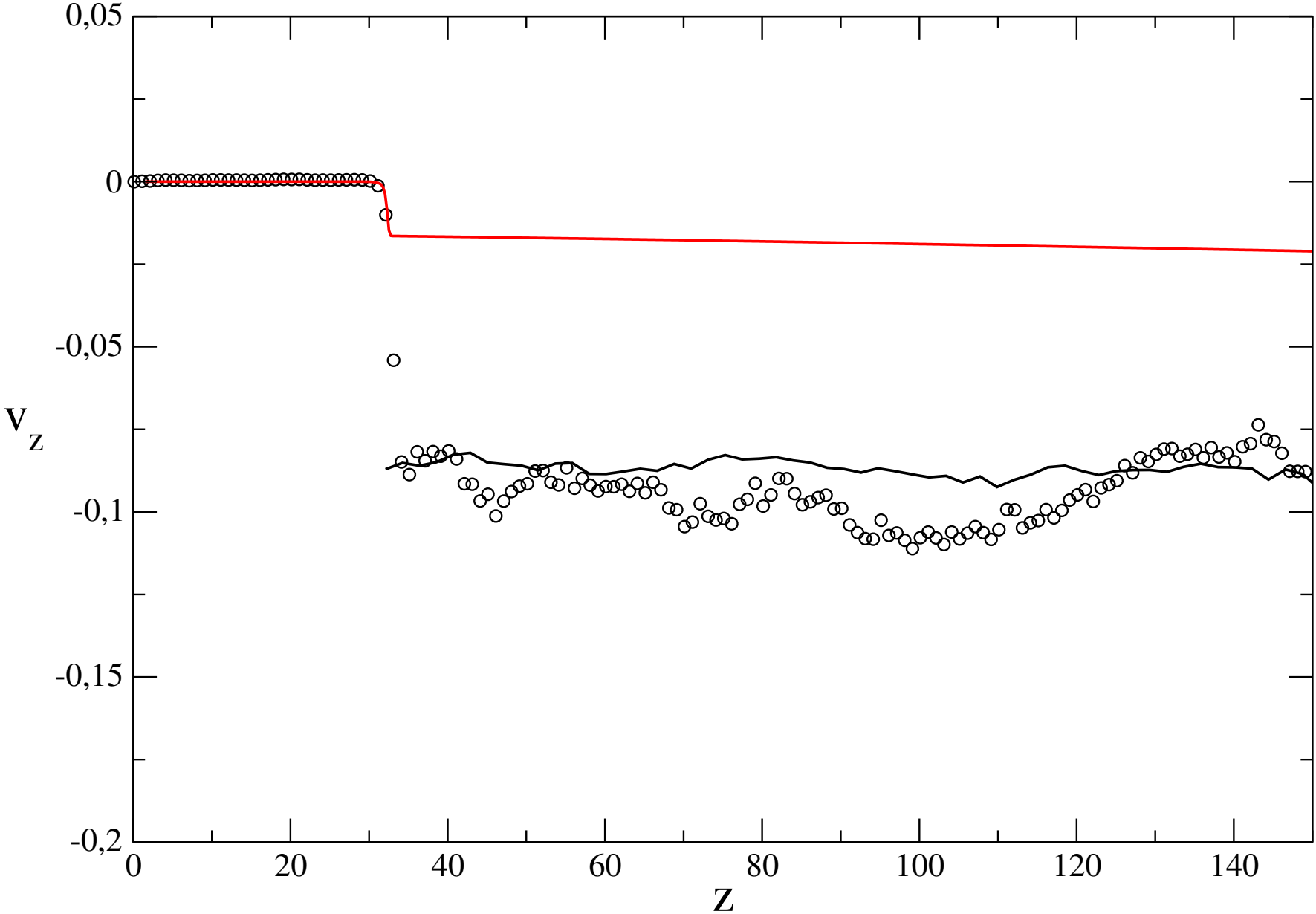
0,05
0
-0,05
-0,1
-0,15
-0,2
V z
0
20
40
60
80
100
120
140
Z

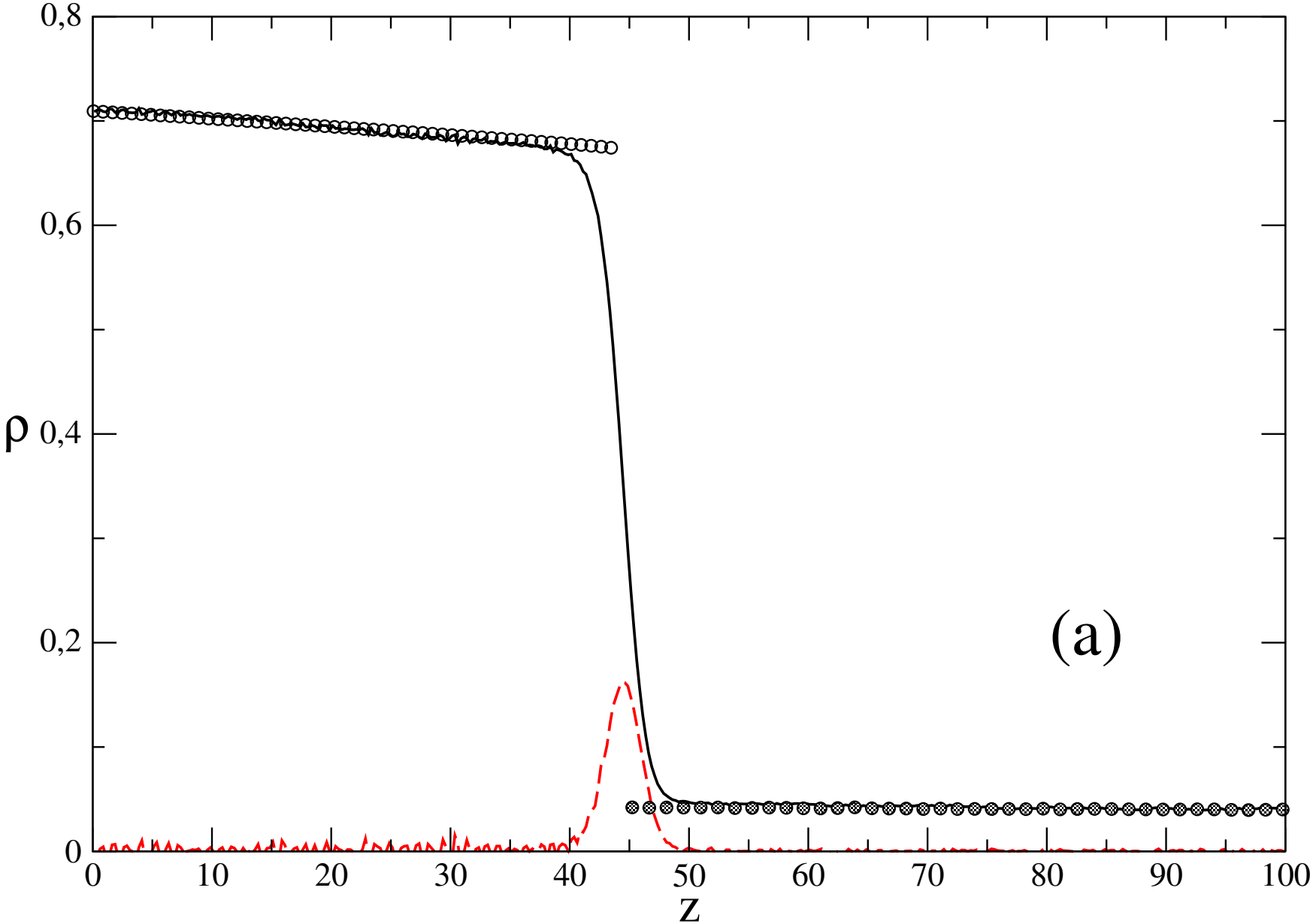
0,8
0,6
0,4
0,2
0
ρ
0
10
20
30
40
50
60
70
80
90
100
z
(a)

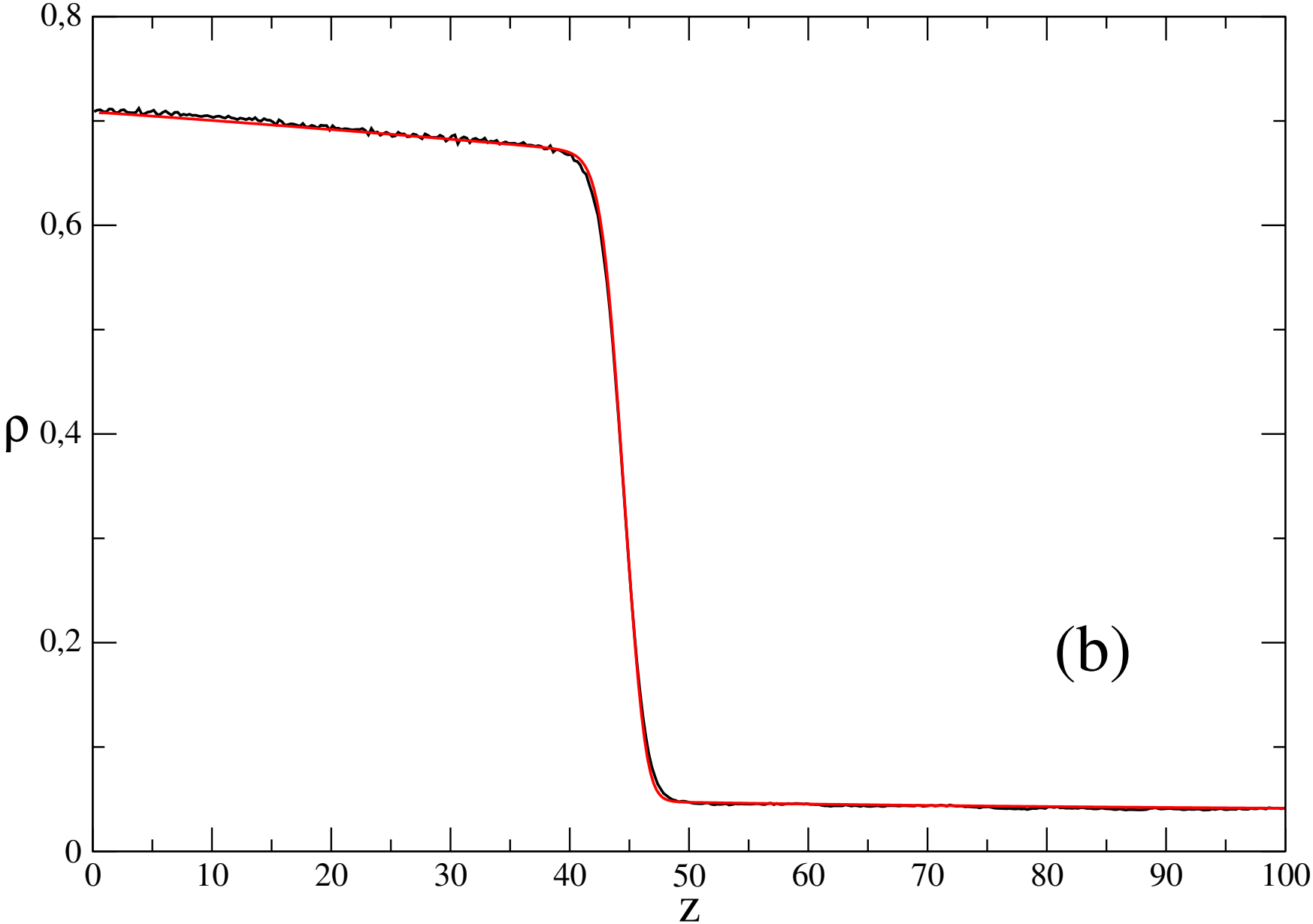
0,8
0,6
0,4
0,2
0
ρ
0
10
20
30
40
50
60
70
80
90
100
z
(b)

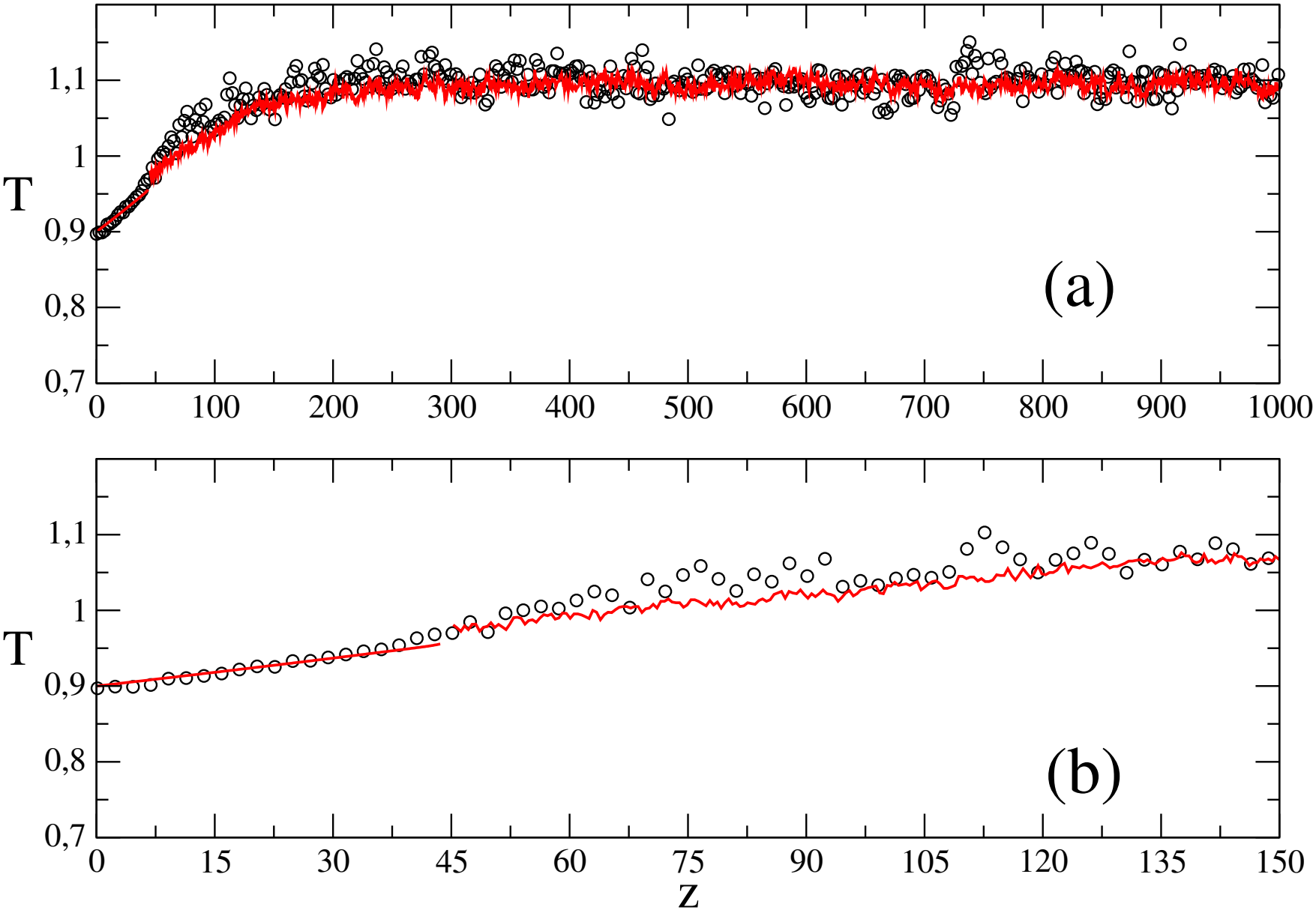
T
1,1
1
0,9
0,8
0,7
0
100
200
300
400
500
600
700
800
900
1000
(a)
T
1,1
1
0,9
0,8
0,7
0
15
30
45
60
75
90
105
120
135
150
z
(b)

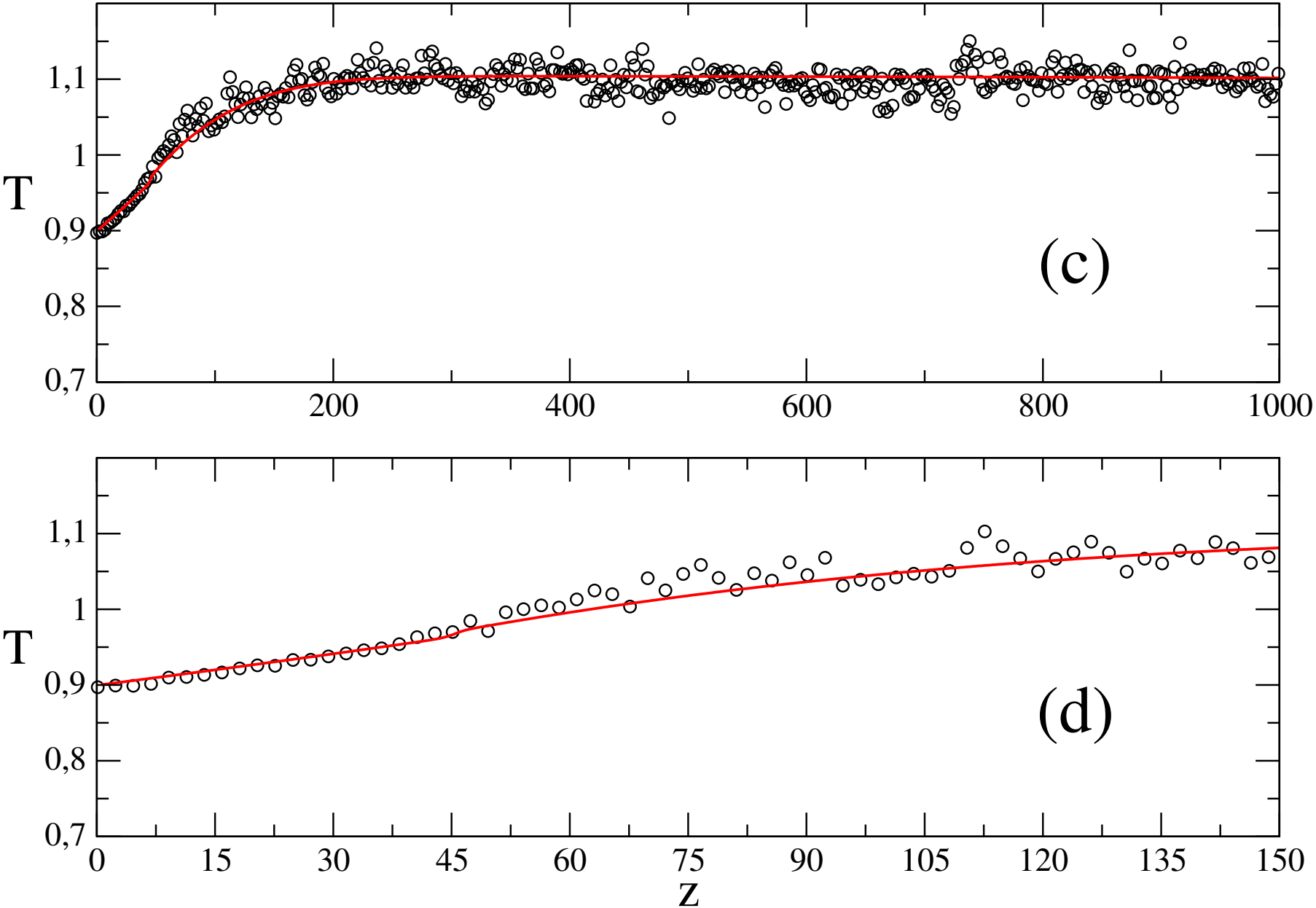
T
1,1
1
0,9
0,8
0,7
0
200
400
600
800
1000
(c)
T
1,1
1
0,9
0,8
0,7
0
15
30
45
60
75
90
105
120
135
150
z
(d)

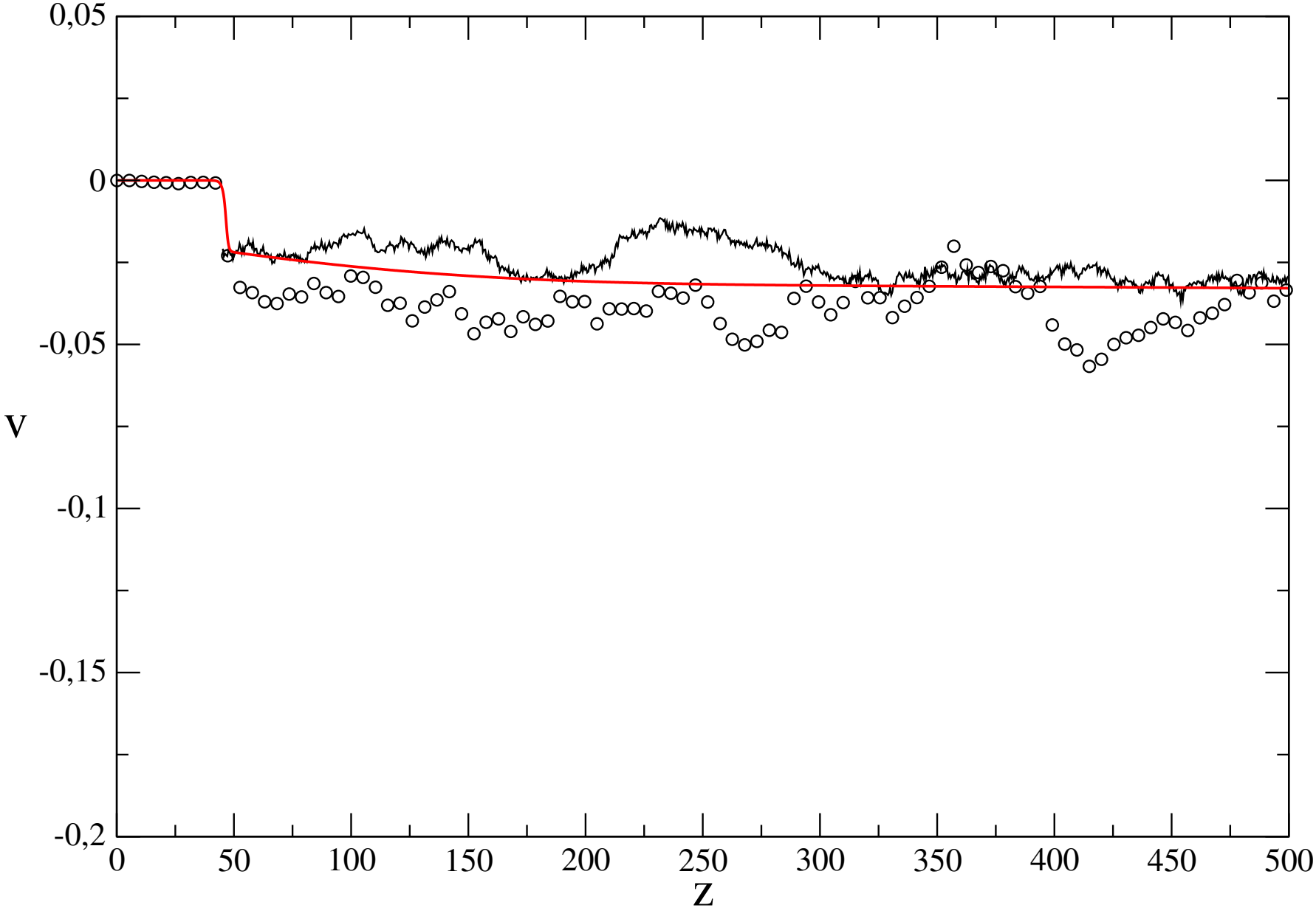
0,05
0
-0,05
-0,1
-0,15
-0,2
V
0
50
100
150
200
250
300
350
400
450
500
Z

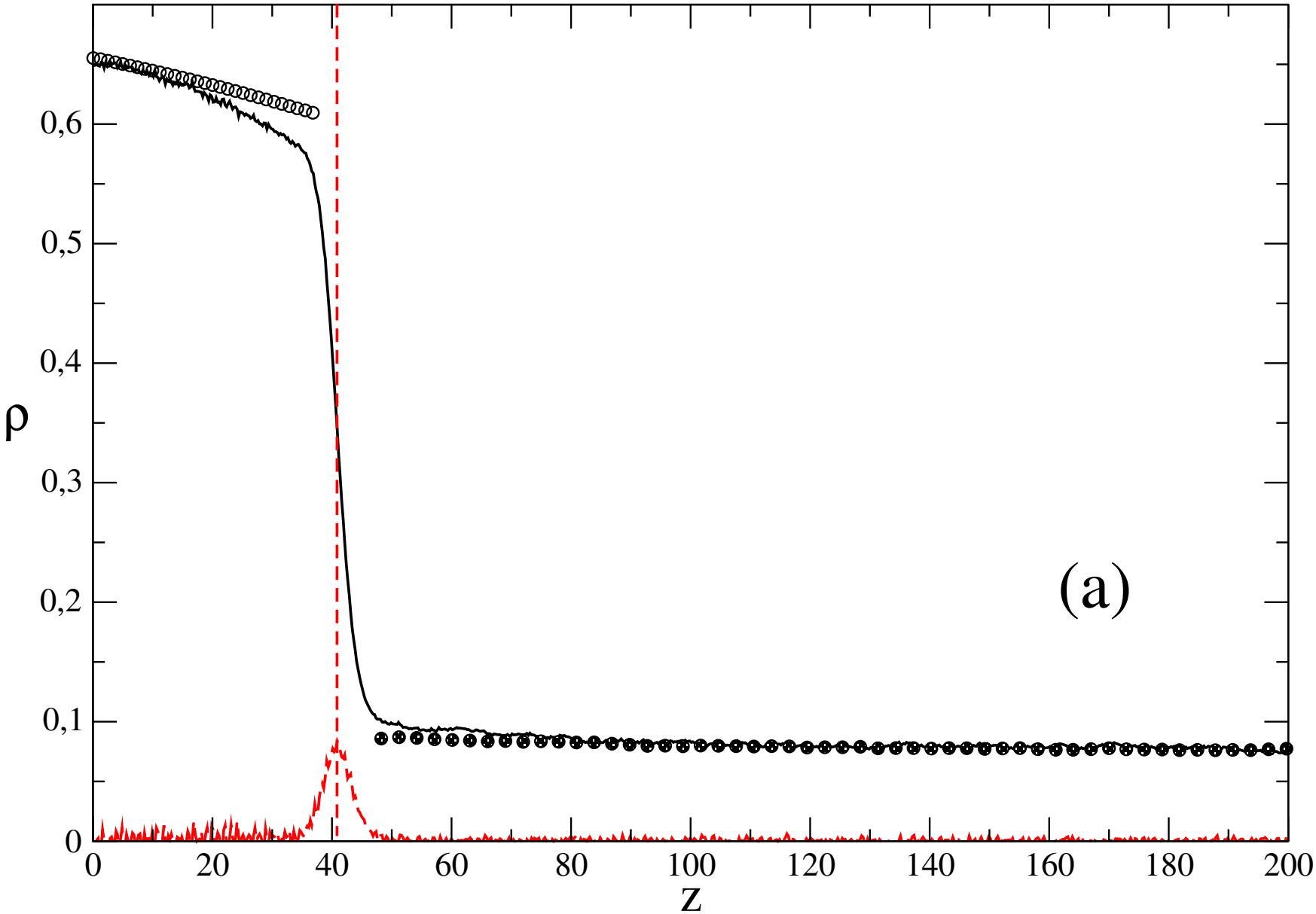
0,6
0,5
0,4
ρ
0,3
0,2
0,1
0
0
20
40
60
80
100
120
140
160
180
200
z
(a)

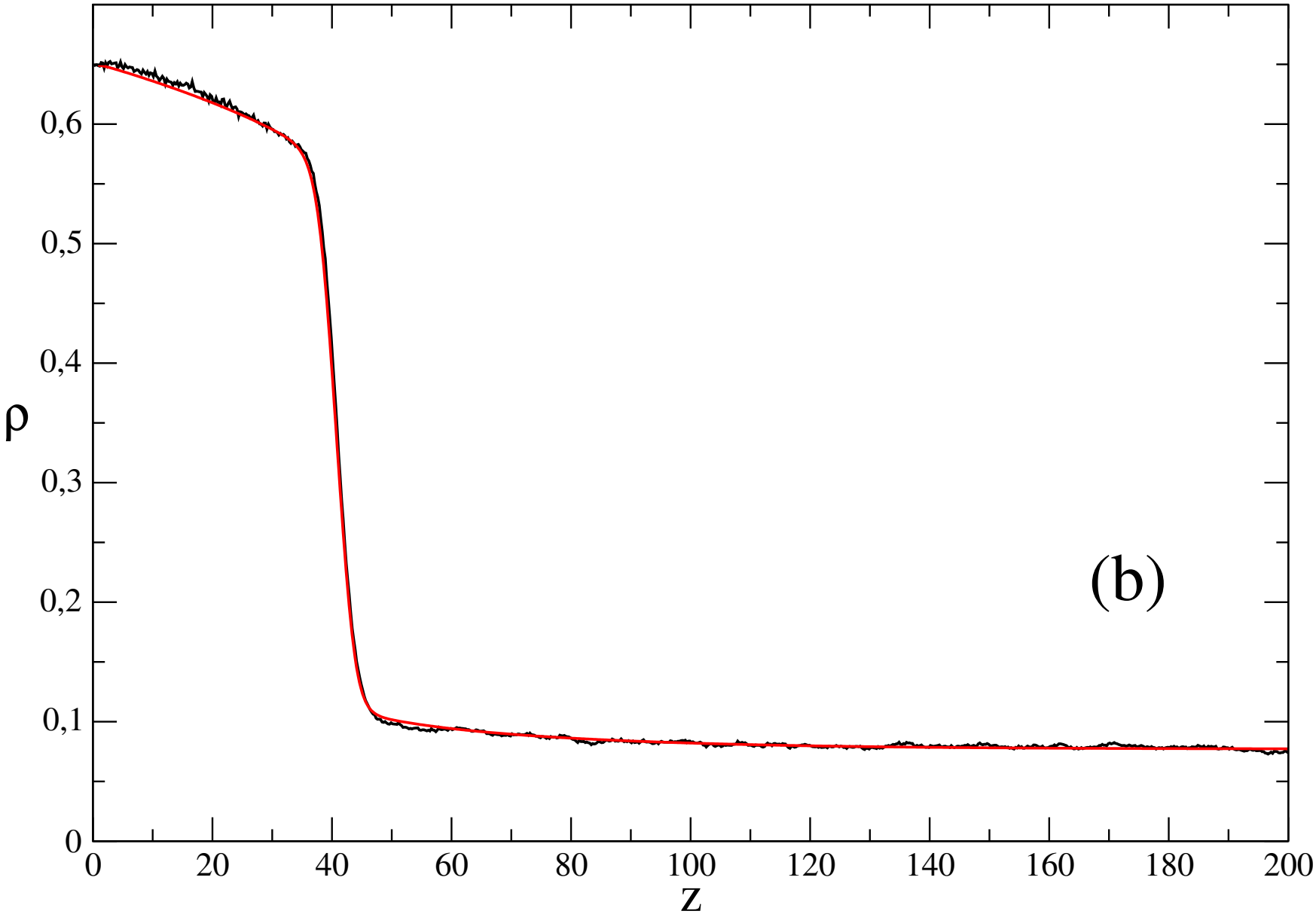
0,6
0,5
0,4
ρ
0,3
0,2
0,1
0
0
20
40
60
80
100
120
140
160
180
200
z
(b)

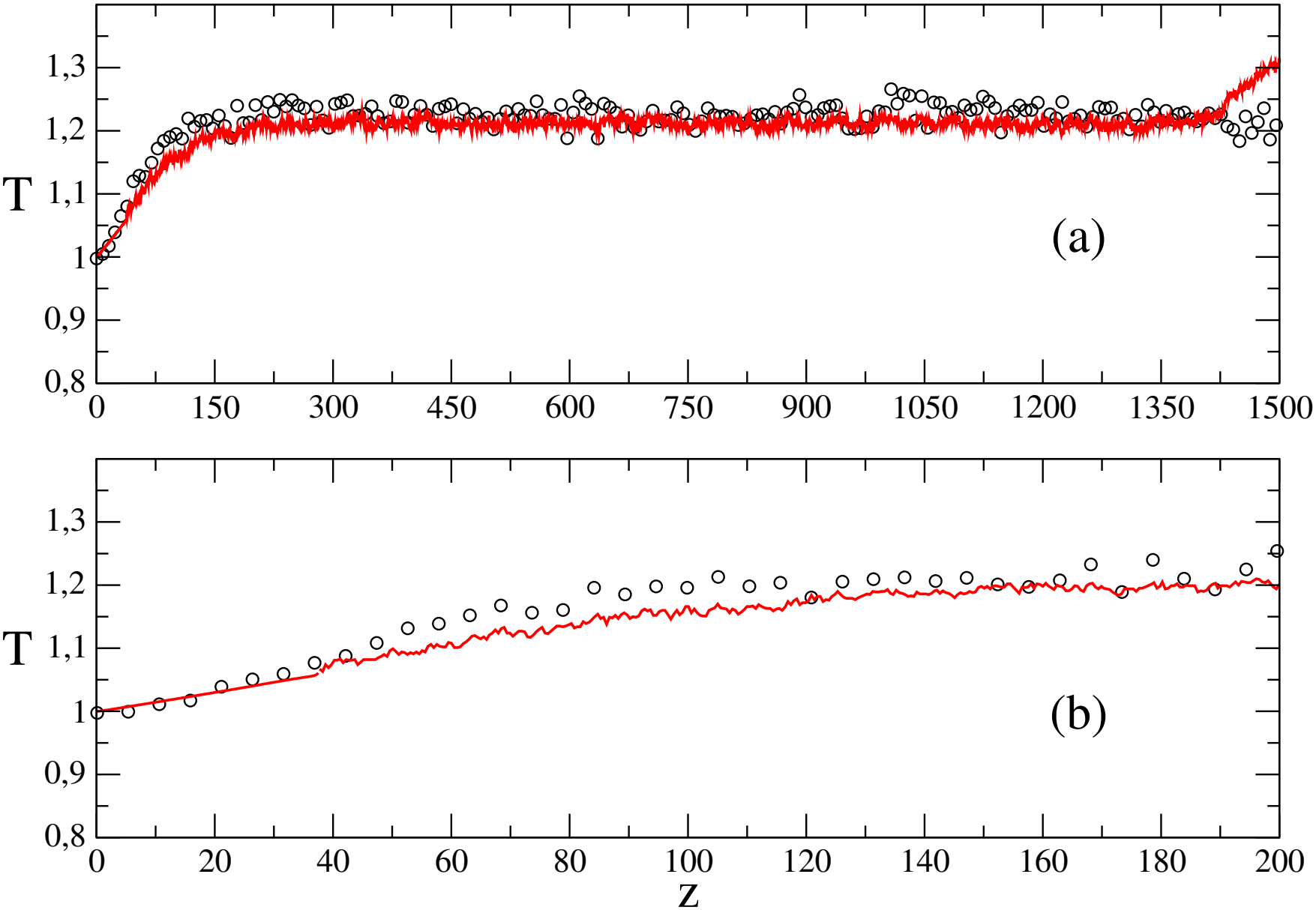
T
1,3
1,2
1,1
1
0,9
0,8
0
150
300
450
600
750
900
1050
1200
1350
1500
(a)
T
1,3
1,2
1,1
1
0,9
0,8
0
20
40
60
80
100
120
140
160
180
200
z
(b)

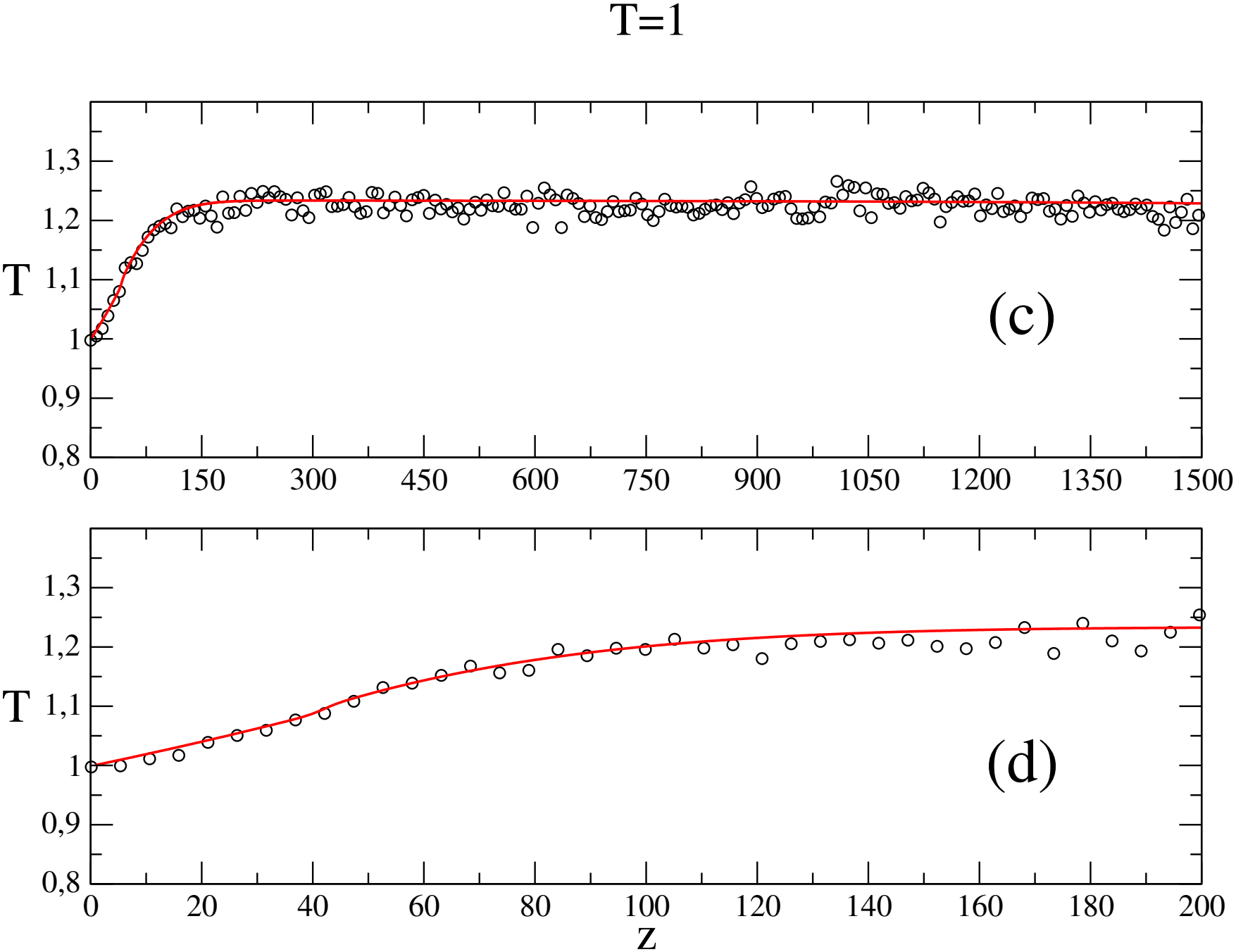
T=1
T
1,3
1,2
1,1
1
0,9
0,8
0
150
300
450
600
750
900
1050
1200
1350
1500
(c)
T
1,3
1,2
1,1
1
0,9
0,8
0
20
40
60
80
100
120
140
160
180
200
z
(d)

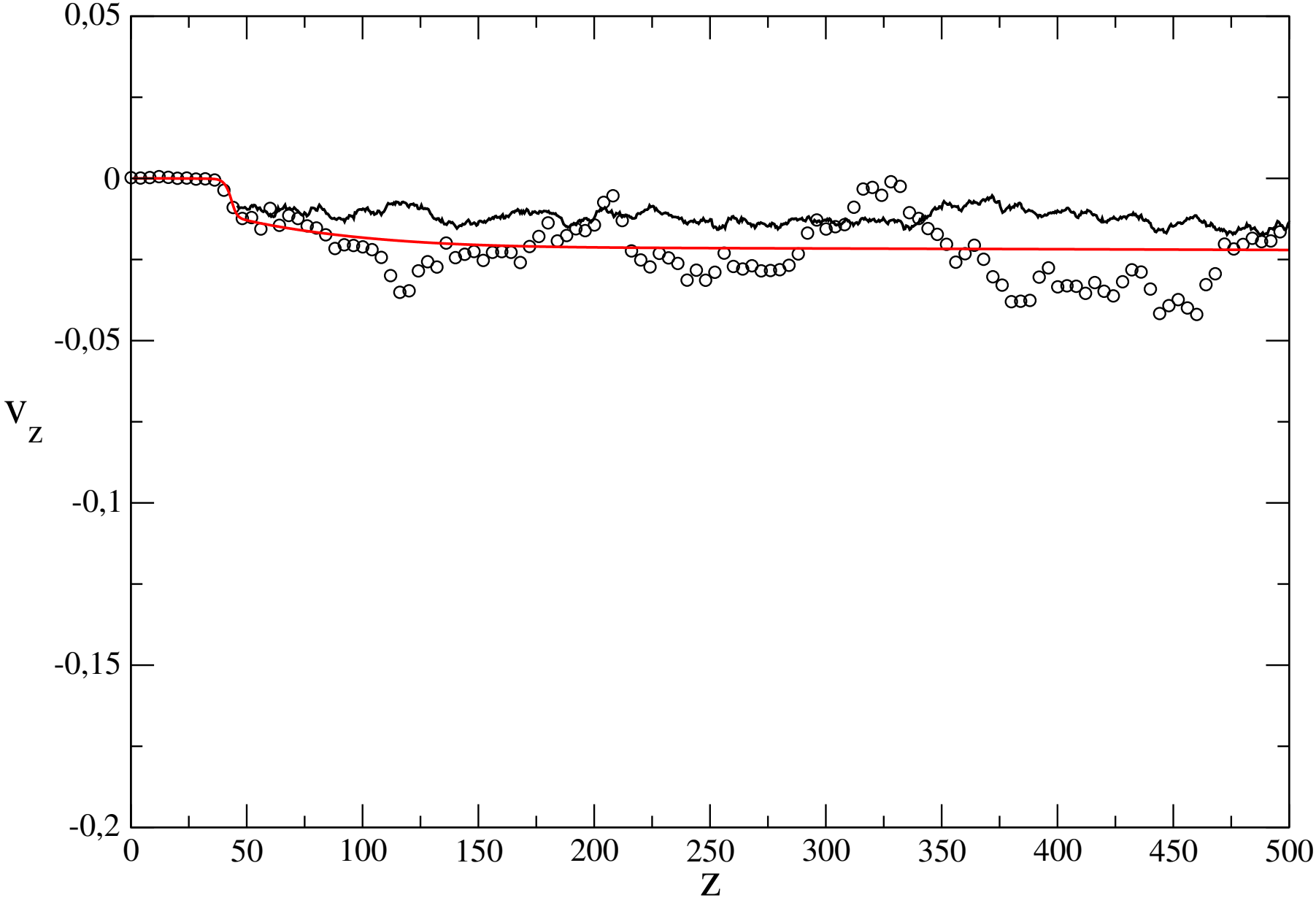
0,05
0
-0,05
-0,1
-0,15
-0,2
V
z
0
50
100
150
200
250
300
350
400
450
500
Z